

NEAR INFRARED SPECTRA AND INTRINSIC LUMINOSITIES OF CANDIDATE TYPE II QUASARS AT $2 < z < 3.4$

JENNY E. GREENE¹, RACHAEL ALEXANDROFF², MICHAEL A. STRAUSS¹, NADIA L. ZAKAMSKA², DUSTIN
LANG³, GUILIN LIU², PETCHARA PATTARAKIJWANICH¹, FREDERICK HAMANN⁴, NICHOLAS P. ROSS⁵,
ADAM D. MYERS⁶, W. NIEL BRANDT^{7,9}, DONALD YORK⁸, DONALD P. SCHNEIDER^{7,9}
Accepted version; April 11, 2014; to be published in The Astrophysical Journal.

ABSTRACT

We present *JHK* near-infrared (NIR) spectroscopy of 25 candidate Type II quasars selected from the Sloan Digital Sky Survey, using Triplespec on the Apache Point Observatory 3.5m telescope, FIRE at the Magellan/Baade 6.5m telescope, and GNIRS on Gemini. At redshifts of $2 < z < 3.4$, our NIR spectra probe the rest-frame optical region of these targets, which were initially selected to have strong lines of C IV and Ly α , with $\text{FWHM} < 2000 \text{ km s}^{-1}$ from the SDSS pipeline. We use the [O III] $\lambda 5007$ line shape as a model for the narrow line region emission, and find that H α consistently requires a broad component with FWHMs ranging from 1000 to 7500 km s^{-1} . Interestingly, the C IV lines also require broad bases, but with considerably narrower widths of 1000 to 4500 km s^{-1} . Estimating the extinction using the Balmer decrement and also the relationship in lower- z quasars between rest equivalent width and luminosity in the [O III] line, we find typical A_V values of 0–2 mag, which naturally explains the attenuated C IV lines relative to H α . We propose that our targets are moderately obscured quasars. We also describe one unusual object with three distinct velocity peaks in its [O III] spectrum.

1. INTRODUCTION

A major stumbling block to understanding the accretion history of supermassive black holes (BHs) over cosmic time is determining the role of obscuration in the demographics of active galactic nuclei (AGN). Optical surveys are quite successful at finding luminous blue (unobscured Type I) quasars (e.g., Richards et al. 2006; Ross et al. 2013), but are not sensitive to truly obscured (or Type II) quasars, where the quasar continuum and broad emission lines are completely hidden. Sensitive 0.5–10 keV X-ray surveys can find modestly obscured systems, but typically cover a limited solid angle, and thus are not sensitive to rare luminous objects (e.g., Brandt & Hasinger 2005; Gilli et al. 2007; Xue et al. 2012; Georgantopoulos et al. 2013). Similar caveats apply to mid-infrared (MIR) selection using *Spitzer* (e.g., Lacy et al. 2004; Stern et al. 2005; Donley et al. 2008, 2012; Lacy et al. 2013), while *WISE* can unambiguously select only the most luminous AGN (e.g., Stern et al. 2012; Assef et al. 2013; Yan et al. 2013). Many X-ray-based studies indicate a decreasing obscured fraction as a function of luminosity over a broad redshift range (e.g., Steffen et al. 2003; Hasinger 2008), but at low redshift ($z < 0.8$), luminous optically selected samples suggest comparable numbers of obscured and unobscured systems (Reyes et al. 2008). At high redshifts, at the peak of quasar activity ($z \simeq 2-3$), demographics are even more uncertain and a large-area survey of luminous obscured quasar activity is required to determine the obscured fraction.

Although unified theories state that Type I and Type II quasars differ only in orientation (e.g., Antonucci & Miller 1985; Antonucci 1993; Urry & Padovani 1995), there are many hints that Type II quasars may represent a special phase in the

growth of black holes. There have been numerous suggestions, both observational (e.g., Sanders et al. 1988; Canalizo & Stockton 2001; Page et al. 2001; Ho 2005; Stevens et al. 2005; Veilleux et al. 2009) and theoretical (e.g., Hopkins et al. 2006), that major galaxy mergers trigger an obscured phase of central BH growth. This obscured phase persists until the AGN grows powerful enough to expel all remaining gas out of the surrounding galaxy, leading to an optically luminous quasar phase. Samples of Type I quasars with moderate extinction hosted by merging galaxies provide some support for this scenario (e.g., Urrutia et al. 2008). Again, larger homogeneous samples of obscured quasars, at the peak epoch of BH growth, are needed to statistically address the growth phase of these objects.

Finally, some obscuration may occur in a torus near the AGN, while some may be due to galaxy-scale dust (Rigby et al. 2006). The torus geometry or porosity may also depend on luminosity (e.g., Steffen et al. 2003; Assef et al. 2013). Larger samples of luminous obscured quasars could address the full distribution of obscuration as a function of bolometric luminosity.

To date, Type II samples at high redshift number in the tens, including targets selected in the radio (e.g., McCarthy 1993; Urry & Padovani 1995; Stern et al. 1999), X-ray (Norman et al. 2002; Stern et al. 2002; Barger et al. 2003; Iwasawa et al. 2012), mid-infrared (Lacy et al. 2004; Stern et al. 2005; Donley et al. 2012; Eisenhardt et al. 2012; Assef et al. 2013; Lacy et al. 2013) and optical (Steidel et al. 2002; Bongiorno et al. 2010; Hainline et al. 2012; Mignoli et al. 2013).

¹ Department of Astrophysical Sciences, Princeton University, Princeton, NJ 08544

² Center for Astrophysical Sciences, Department of Physics and Astronomy, Johns Hopkins University, Baltimore, MD 21218, USA

³ McWilliams Center for Cosmology, Department of Physics, Carnegie Mellon University, Pittsburgh, PA, USA

⁴ Department of Astronomy, University of Florida, Gainesville, FL 32611-2055, USA

⁵ Department of Physics, Drexel University, 3141 Chestnut Street, Philadelphia, PA 19104, USA

⁶ Department of Physics and Astronomy, University of Wyoming, Laramie, WY 82071, USA

⁷ Department of Astronomy and Astrophysics, The Pennsylvania State University, 525 Davey Lab, University Park, PA 16802 USA

⁸ University of Chicago Astronomy and Astrophysics Department and Enrico Fermi Institute, 5640 So. Ellis Ave., Chicago, 60637

⁹ Institute for Gravitation and the Cosmos, The Pennsylvania State University, University Park, PA 16802

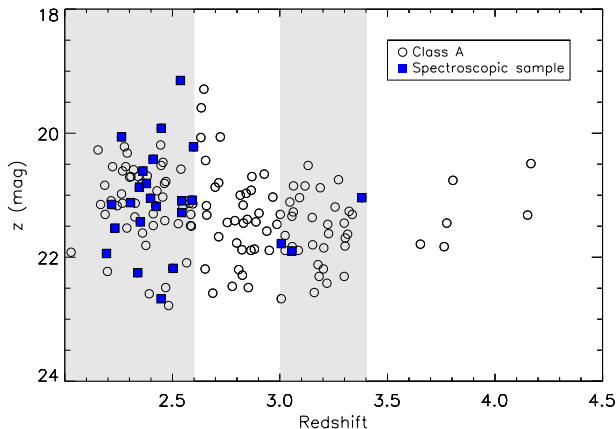


FIG. 1.— Redshift vs. z -band magnitude for the Alexandroff et al. Class A objects (open) and the sample spectroscopically targeted in the NIR (blue squares). Shaded bands indicate redshift regions where strong rest-frame optical emission lines fall in atmospherically transparent regions of the spectrum. Our spectroscopic subsample is representative of the full distribution.

The operational definition of obscured quasar depends on the selection technique. The typical X-ray definition of H I column density $N_H > 10^{22} \text{ cm}^{-2}$ (e.g., Ueda et al. 2003) apparently corresponds to an $A_V \approx 0.47$ in AGN (Maiolino et al. 2001; Assef et al. 2013). In contrast, optically selected Type II Seyfert galaxies typically have $A_V > 10$ (e.g., Veilleux et al. 1997; Zakamska et al. 2005). Finally, near-infrared selection criteria yield moderately reddened quasars with broad $H\alpha$ and typical $A_V \sim 0.3 - 6$ (e.g., Banerji et al. 2012; Glikman et al. 2012).

In this paper, we focus on Type II candidates selected in the rest-frame UV, to explore the A_V distribution of objects selected on the basis of narrow UV emission lines. Low-redshift ($z < 0.8$) Type II quasars were successfully discovered in large numbers in the Sloan Digital Sky Survey (SDSS; York et al. 2000) based on their strong and narrow [O III] $\lambda 5007\text{\AA}$ emission (Zakamska et al. 2003; Reyes et al. 2008), and subsequently shown to be bona fide obscured quasars (Zakamska et al. 2005, 2006, 2008). Not until the Baryon Oscillation Spectroscopic Survey (BOSS; Eisenstein et al. 2011; Dawson et al. 2013), which spectroscopically targeted quasars down to a magnitude limit of $g < 22$ or $r < 21.85$ (Ross et al. 2012), did it become possible to select Type II quasar candidates with $z > 1$ with the SDSS. In Alexandroff et al. (2013, hereafter Paper I) and this work, high redshift Type II quasar candidates are identified based on the presence of strong and narrow high-ionization lines in their rest-frame UV spectra (e.g., C IV).

In Paper I, we presented a sample of 145 Type II quasar candidates selected from the BOSS survey based on their narrow ($< 2000 \text{ km s}^{-1}$) C IV and Ly α emission. The narrow linewidths and high rest equivalent widths (EWs) of the sample objects bear strong resemblance to those of other samples of Type II quasars. Furthermore, in the two objects we observed with a spectropolarimeter, we detected continuum polarization of $\sim 3\%$, inconsistent with typical unobscured quasars. On the other hand, our BOSS Type II quasar candidates are too luminous and blue in the UV continuum to be explained by galaxy light alone. They have typical rest-frame UV continuum luminosities of -24 AB mag at 1450\AA , as compared to magnitudes of ~ -22.5 AB mag (Oke & Gunn 1983) for the most luminous UV-selected galaxies at similar redshifts (Shapley 2011).

The AGN must contribute some UV light, whether it be directly transmitted or due to scattered light. Furthermore, the UV line ratios are more akin to Type I rather than Type II objects. Finally, in one object with broad spectral energy distribution (SED) coverage, the optical/UV is weaker than seen in typical Type I objects indicating some obscuration, but more prominent than in typical Type II objects. In the same sense, the optical/NIR colors of our Type II candidates are similar to unobscured quasars. Thus, based on the rest-frame UV spectra alone, it is difficult to determine the true nature of these sources.

Here, we present NIR spectroscopy that probes the rest-frame optical spectra of 25 of the Type II quasar candidates presented in Paper I. We use three NIR echellettes, Triplespec (Wilson et al. 2004) on the 3.5m at Apache Point Observatory (APO), the Folded-port InfraRed Echellette (FIRE; Simcoe et al. 2013) at Magellan, and Gemini Near Infrared Spectrograph (GNIRS; Elias et al. 2006) on Gemini North, all three of which afford us JHK spectroscopy in a single observation. We simultaneously measure $H\beta$, $H\alpha$, and the strong and ubiquitous [O III] $\lambda 5007$ line in the majority of our targets. The [O III] line luminosity is known to correlate with the intrinsic luminosity of the quasar (Yee 1980; Heckman et al. 2004; Liu et al. 2009), while the strength and width of the Balmer lines provide new insight into the level and scale of the extinction. Finally, the [O III] line shape unambiguously traces the low-density (narrow-line region) gas kinematics, and thus allows us to characterize any additional (broader) components in the permitted lines. In fact, we specifically targeted two galaxies with multiple velocity peaks in the C IV and/or Ly α line (Paper I), to determine whether the peaks are caused by absorption or real kinematic structure in the gas.

The paper proceeds as follows. In §2 we present properties of the sample and details of the observations. In §3 we discuss the data reduction, while in §4 we outline our line-fitting technique. We present our results in §5, and discuss the implications for obscured quasars in §6. We assume a concordance cosmology with $H_0 = 70 \text{ km s}^{-1} \text{ Mpc}^{-1}$, $\Omega_M = 0.3$, and $\Omega_\Lambda = 0.7$ (Dunkley et al. 2009).

2. SAMPLE DESCRIPTION AND OBSERVATIONS

Our parent Type II sample is discussed in detail in Alexandroff et al. (2013); we summarize our selection criteria briefly here. We started with SDSS/BOSS spectra (Gunn et al. 2006; Smee et al. 2013), first released in the 9th Data Release (DR9; Ahn et al. 2012; P aris et al. 2012), and selected all the SDSS/BOSS objects in DR9 with both Ly α and C IV in the spectra (corresponding to $z > 2.0$), a reliable spectroscopic pipeline fit (i.e., the flag ZWARNING = 0; Bolton et al. 2012) and 5σ detections in both Ly α and C IV. We selected the targets with FWHM (C IV and Ly α) $< 2000 \text{ km s}^{-1}$; while somewhat arbitrary, this cut is designed based on observations of luminous Type II quasars at $z \approx 0.5$ (Greene et al. 2011; Liu et al. 2013a,b). The BOSS spectrum of each candidate was then visually inspected. Objects with extreme absorption features are classified as broad absorption line (BAL) quasars (14% of the narrow-line objects), while those with strong permitted Fe emission and strong blue continua were classified as narrow-line Seyfert 1 galaxies (NLS1s; e.g., Osterbrock & Pogge 1985, 56% of the narrow-line objects). After removing these two classes, the resulting sample comprises 452 objects that are strong or possible cases for Type II quasars.

Even after removing the most obvious BALs and NLS1s,

Table 1. Sample and Observations

Quasar Name (SDSS) (1)	RA (2)	Dec (3)	z_{UV} (4)	z_{opt} (5)	i -band (6)	Tel. (7)	Date (8)	Exp. (9)
J022051.68-012403.3	35.21532	-1.4009	2.5978	2.5989	20.73	APO	12/27/11	2880
J023359.27+005925.8	38.49696	0.9905	2.5441	...	21.96	APO	11/16/11	3840
J073637.54+225917.4	114.15642	22.9882	2.2630	2.2643	20.44	APO	12/27/11	4800
J073851.85+424010.9	114.71599	42.3364	2.1870	2.1883	21.94	Gemini	02/03/12	3600
J081257.15+181916.8	123.23812	18.3213	2.3786	2.3794	21.35	APO	12/27/11	3820
J082530.67+120658.4	126.37778	12.1162	2.3507	...	22.47	APO	03/15/12	3820
J090612.64+030900.4	136.55268	3.1501	2.5001	...	21.72	Magellan	03/10/12	3635
J091301.33+034207.6 ^b	138.25556	3.7021	3.0060	3.0058	21.78	Magellan	03/09/12	3635
J095118.93+450432.4	147.82886	45.0757	2.4469	2.4454	20.87	APO	12/27/11	3820
J095819.35+013530.5	149.58064	1.5918	3.0554	3.0544	21.50	Magellan	03/08/12	3635
J103249.55+373649.0	158.20644	37.6136	2.3460	2.3516	21.51	APO	03/15/12	3820
J115510.34+044455.4	178.79309	4.7487	2.4240	2.4210	21.77	Magellan	03/10/12	3635
J130907.83+020547.6 ^a	197.28264	2.0966	2.2325	2.2258	21.47	Magellan	03/10/12	2726
J133059.32+014610.3	202.74718	1.7695	2.3384	2.3405	22.41	Magellan	03/10/12	3635
J133927.80+044158.0	204.86585	4.6994	2.5911	2.5874	21.62	Magellan	03/09/12	2420
J134240.84-004540.6 ^a	205.67015	-0.7613	2.3050	2.3031	21.12	Gemini	05/28/12	3600
J140625.75+042919.4	211.60730	4.4887	3.3806	3.3802	20.74	Magellan	03/09/12	3635
J144441.05-001343.4	221.17104	-0.2287	2.5430	2.5479	21.75	Magellan	03/08/12	3635
J151544.01+175753.0	228.93337	17.9647	2.3980	...	21.89	APO	06/02/12	3820
J154640.45-000328.3	236.66854	-0.0579	2.2168	...	21.63	Magellan	03/08/12	3022
J160900.01+190534.8	242.25005	19.0930	2.5395	2.5395	21.28	Gemini	05/02/12	3600
J170558.64+273624.8	256.49434	27.6069	2.4480	...	20.71	APO	06/02/12	4800
J215341.33+041132.7	328.42221	4.1924	2.4098	2.4115	20.96	APO	11/16/11	6720
J222946.61+005540.5	337.44419	0.9279	2.3623	2.3628	21.08	APO	11/16/11	5760
J225252.70+010829.6 ^a	343.21960	1.1416	2.5370	2.5291	19.89	APO	08/23/11	5760

Note. — Col. (1): Official SDSS-BOSS name. Object marked with 'a' fell out of the final Class A sample from Alexandroff et al. (2013). Object marked with 'b' was also observed by Gemini. Throughout the text we will refer to targets with an abbreviated name (e.g., SDSS J0220-0124). Col. (4): Right Ascension (deg; J2000). Col. (5): Declination (deg; J2000). Col. (2): Redshift adapted from Pâris et al. (2012) as described in Paper I. Col. (3): Redshift of the [O III] line; if no measurement, we detected neither emission lines nor continuum from the NIR spectrum. Col. (6): Observed i -band PSF magnitude from SDSS. Col. (7): Telescope. Col. (8): Observation date (UT). Col. (9): Exposure time (sec).

some objects still appeared ambiguous (for instance, the C IV line had a broad base). Those most likely to be Type II quasars were classified as Class A (145 objects), while the ambiguous sources were classified as Class B (307 objects). As shown in Paper I, this visual classification separates the sources by linewidth and continuum strength, although ultimately it is somewhat subjective. The median FWHM of the CIV line among the Class A candidates is $\langle \text{FWHM} \rangle = 1260 \text{ km s}^{-1}$. The mean redshift of these two samples is $\langle z \rangle = 2.70$, with a redshift range from 2.03 to 4.23. Almost all the objects in both Class A and Class B were selected for spectroscopy as quasar candidates, using the algorithms described in Ross et al. (2012), with only four Class A candidates selected under various auxiliary programs (e.g., a color-based high-redshift quasar search).

All but three of the objects presented here are Class A targets. There are three exceptions that do not appear in Paper I, but were selected in an early version of this work using less stringent C IV and Lyman α restrictions. In total, we have obtained NIR spectra for 12 objects with APO, 10 with Magellan, and three additional objects (plus one repeated object) with Gemini (Table 1). The final 25 targets span the luminosity and redshift range of the full sample. Type II quasar candidates were selected for NIR spectroscopic observation based on a number of criteria, and the sample is summarized in Figure 1. Since many Type II quasars in the literature have been found via radio selection, we focused on the majority of targets that are undetected in FIRST (comprising 98% of the class A sample; Becker et al. 1995), although given the limited FIRST sensitivity and the faint UV continua, we cannot rule out that many of the non-radio detections are actually radio loud. We then se-

lected targets in the redshift ranges $2 < z < 2.6$ or $3.0 < z < 3.4$, to ensure that the emission lines of interest, H β , [OIII] and H α (at low redshift), fell into windows of high atmospheric transparency. Within these wavelength windows, we further selected windows where none of the strong emission lines coincide with strong sky emission lines. Finally, we targeted two interesting targets with multiple velocity components in both the Ly α and C IV lines (§5.5). From the UV spectra alone, we suggested that the observed velocity structure of the CIV line was likely due to superposed absorption features (Paper I). Another possibility was that the multiple peaks corresponded to multiple physical components, perhaps in the process of forming a new galaxy. Our NIR spectra allow a test of these hypotheses.

For the Triplespec targets, we additionally imposed a z -band magnitude limit of $z < 21$, such that we could identify targets in the guider (although occasionally blind offsets were used to place the target in the slit). For the FIRE data, we prioritized fainter targets, down to $z \approx 22.7$ mag. In cases where multiple targets satisfied these criteria, priority was given to those with matches in various X-ray surveys, those in our approved *HST* imaging program, and those with the multi-peaked emission lines described above. Finally, we prioritized those few targets with nearby tip-tilt stars for future adaptive-optics observation. Below we describe the observations taken with each instrument individually.

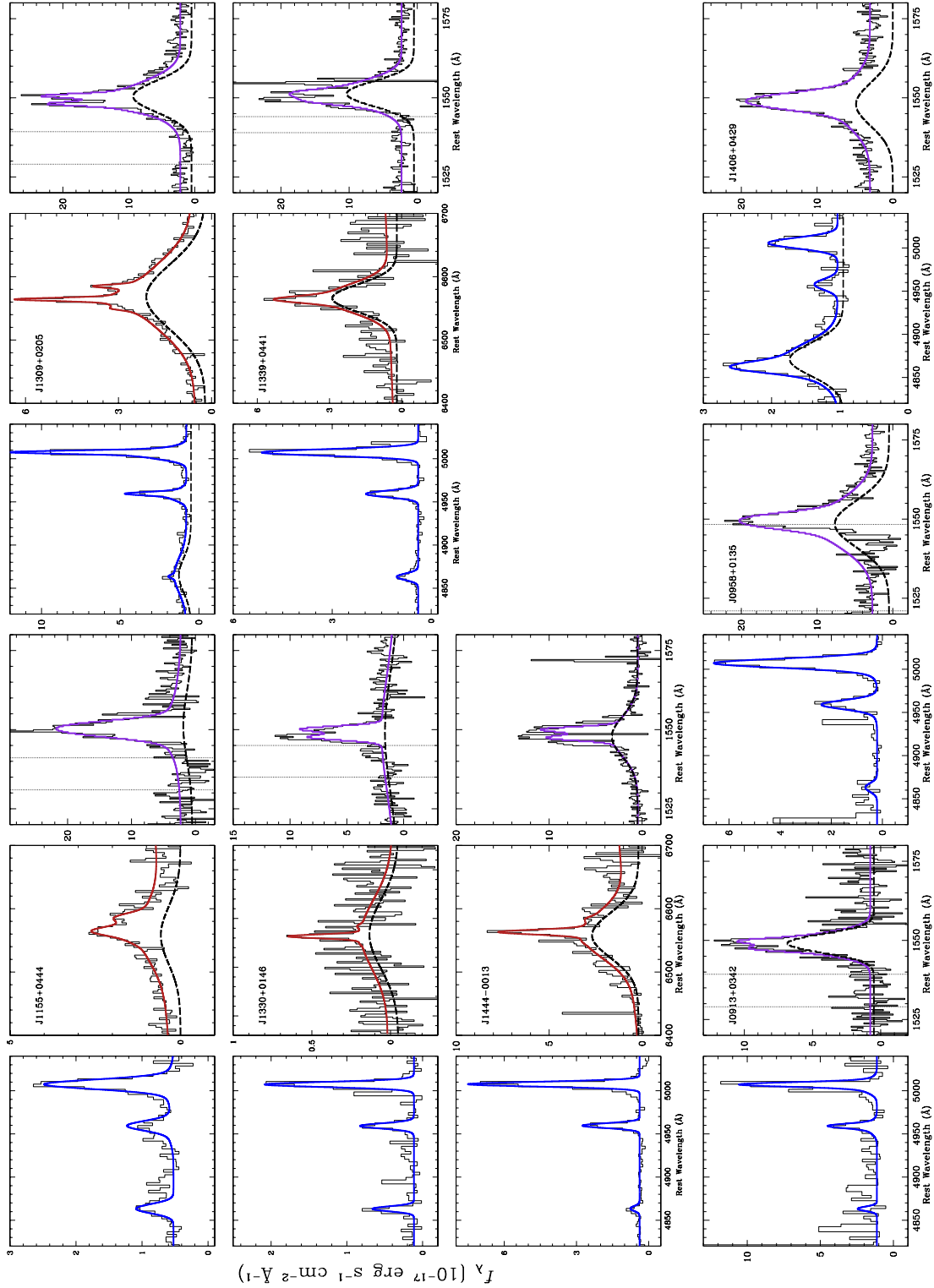


FIG. 2.— The top three rows show fits to the [O III], H α , and C IV regions of all five of the Magellan spectra with H α in the spectral region, while the C IV is from the SDSS spectra. In the bottom row, we present the three higher redshift targets for which H α was not observed. The original spectra are binned by three pixels (thin black solid lines), and our best overall model fit (thick blue, red, or magenta solid lines for [O III], H α , and C IV respectively), and when present the broad components are shown offset for clarity (thick dotted lines). In the fits to the H α and C IV regions, the narrow component is constrained to match the [O III] model shape. The dashed vertical lines indicated the regions that were masked in fitting C IV. See §4 for details.

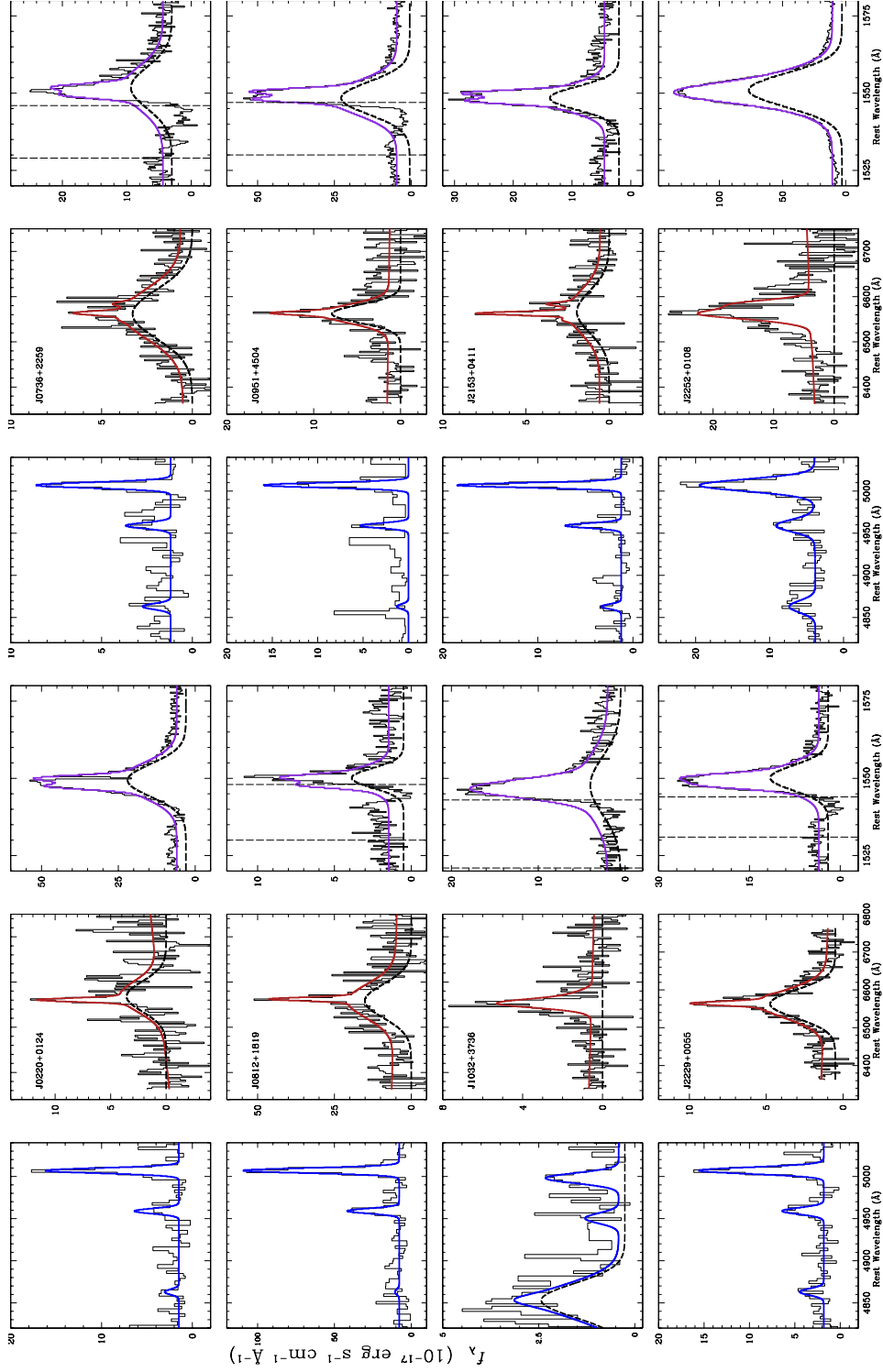


FIG. 3.— Same as Figure 2 above, but for twelve galaxies observed with APO/Triplespec. We show the original spectra in units of $10^{-17} \text{ erg s}^{-1} \text{ cm}^{-2} \text{ \AA}^{-1}$ (thin black solid lines), our best overall model fit (thick blue solid lines), and when present the broad components are shown offset for clarity (thick dotted lines). In the case of the $\text{H}\alpha$ and C IV regions, the narrow component is constrained to match the $[\text{O III}]$ model shape. The dashed vertical lines indicated the regions that were masked in fitting C IV . See §4 for details.

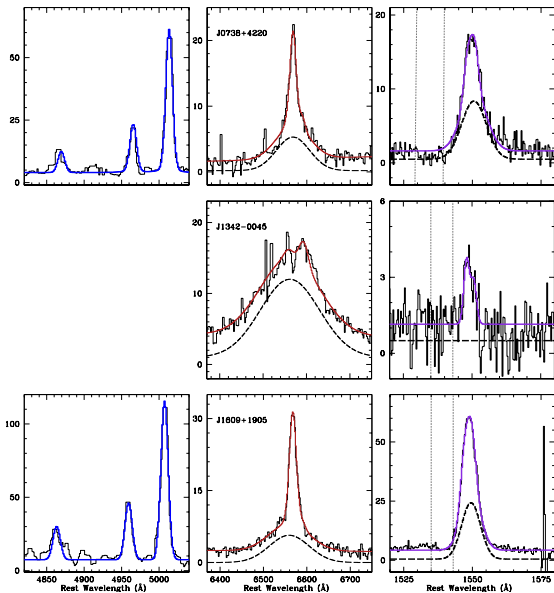


FIG. 4.— As in Figure 2 and Figure 3 above we show the $H\beta$ (left) and $H\alpha$ (center) regions of the spectra taken with Gemini and the CIV region (right) as observed by the SDSS. The y-axis scalings are arbitrary since we have not flux calibrated the Gemini data. We display the unbinned data (black histogram), the models (in blue, red, and magenta respectively), and any broad component to the $H\alpha$ and CIV (dashed). In the case of J1342–0045, no narrow $[OIII]$, $H\beta$, or $H\alpha$ is detected and even the CIV is weak, but broad $H\alpha$ is quite prominent.

2.1. Triplespec

Triplespec is a cross-dispersed NIR spectrograph (Wilson et al. 2004) mounted on the Apache Point 3.5m telescope in New Mexico. It observes simultaneously from $0.95 \mu\text{m}$ to $2.46 \mu\text{m}$ (separated into five spectral orders) with a spectral resolution of $R \approx 5000$. We used a $1''.1$ or $1''.5$ slit depending on observing conditions. To maximize the signal-to-noise ratio for our relatively long exposure times, we used Fowler=8 sampling.

We targeted 12 of our candidates using the Triplespec instrument. The data were taken over the course of four nights: August 23, November 15, and December 26 2011 and March 14 2012 (Table 1). Of the 12 objects that we targeted for spectroscopy, we succeeded in detecting line and/or continuum emission for eight. In the following discussion, we will focus only on the detected targets. However, we do note that we preferentially failed to detect fainter targets (with $i \gtrsim 22$ mag). On the other hand, we have succeeded in detecting sources at these faint magnitudes with Magellan and Gemini.

We observed with a standard ABBA sequence to facilitate sky subtraction, with individual exposure times of 240 sec. We observed each target over the course of 1-2 hours, for total on-source exposure times of 1-1.5 hours (Table 1). We bracketed each target with observations of a telluric standard, typically an A0V star with magnitudes of $V \approx 7$ to 9 mag, at a similar airmass (e.g., Cushing et al. 2004). This star is used both to remove telluric absorption and as a flux calibrator.

2.2. Folded-port Infrared Echellette

The Folded-port Infrared Echellette (FIRE; Simcoe et al. 2013) is a NIR spectrograph used on the 6.5m Baade-Magellan Telescope. In high-resolution mode, it simultaneously observes from $0.8 \mu\text{m}$ to $2.5 \mu\text{m}$ over 21 spectral orders with a spectral resolution of 50 km s^{-1} or $R \approx 6000$ for the $0''.75$ slit that we used. Typical exposure times were 900 sec. In this case

we adopted the Sample Up The Ramp (SUTR) observing technique. SUTR samples the array continuously and the signal is derived as a fit to the accumulated charge over the elapsed time, reducing the read noise significantly. SUTR also has smaller overheads than Fowler Sampling. Our FIRE data were obtained over three half nights on March 7-9 2012. The conditions were good to excellent, with typical seeing of $0''.6$ in the optical. As above, we used a standard ABBA observing sequence and bracketed our science exposures with A0V standard stars, and we typically spent 1 hour of on-source time per target.

2.3. Gemini Near-infrared Spectrograph

We obtained near-infrared spectra of four objects with the Gemini Near-Infrared Spectrograph (GNIRS; Elias et al. 2006) on the Gemini North 8.1 meter telescope on the summit of Mauna Kea, Hawaii. We used the 32 l/mm grating with a cross-dispersion and a $0''.45$ slit, giving a resolution of $R \approx 1200$, and covering the full wavelength range of the J , H , and K bands. The objects were chosen with redshifts such that $H\alpha$ and the $H\beta$ -[O III] complex fell in regions of high atmospheric transparency. Each object was observed in queue mode for a total of 60 minutes in a series of noded exposures along the slit for 300 seconds each, under non-photometric conditions of moderate seeing.

3. REDUCTIONS

The data reduction utilized pipelines described in Vacca et al. (2003) and Cushing et al. (2004) for Triplespec and Simcoe et al. (2012) for FIRE. The Gemini spectra were reduced and calibrated using the Gemini package for IRAF, following the standard example script for GNIRS long-slit observations described in the task *gnirsexamples*. We describe the overall procedure utilized for all data sets, highlighting any differences. In brief, dome flats were obtained and combined in a standard manner, including dark subtraction, to perform a flat-field correction. Wavelength calibration was based on the airglow OH lines from the Earth's atmosphere; wavelength solutions are derived for each target individually. The FIRE pipeline performs a 2D fit to the spatial curvature following Kelson (2003).

We extract our targets as unresolved point sources. AB pairs are differenced to remove airglow emission lines, and then each spectrum is extracted. Extraction positions are determined for each exposure due to occasional drift of the object position from exposure to exposure in the Triplespec data, and then all AB pairs are summed (or median-combined in the case of the Gemini spectra). Telluric correction proceeds in an identical manner in the Triplespec and FIRE pipelines (Vacca et al. 2003). We create a telluric correction spectrum by smoothing and scaling the spectrum of Vega to match the observed standard star; dividing by this model leaves a telluric correction spectrum. The model is shifted in velocity and then the target spectrum is divided by this matched telluric spectrum. Flux calibration based on published photometry of the star is performed simultaneously. All orders are merged and bad pixels are removed. Finally, the spectra are binned onto a uniform wavelength grid. The Gemini data are not flux calibrated.

The nominal K -band magnitudes, as estimated from our spectra, range from $K_{AB} \approx 21.5$ to 18.8 mag. In order to verify the flux calibration of our near-infrared spectra from APO and Magellan we matched our sample with the UKIRT Infrared Deep Sky Survey (UKIDSS; Lawrence et al. 2007).

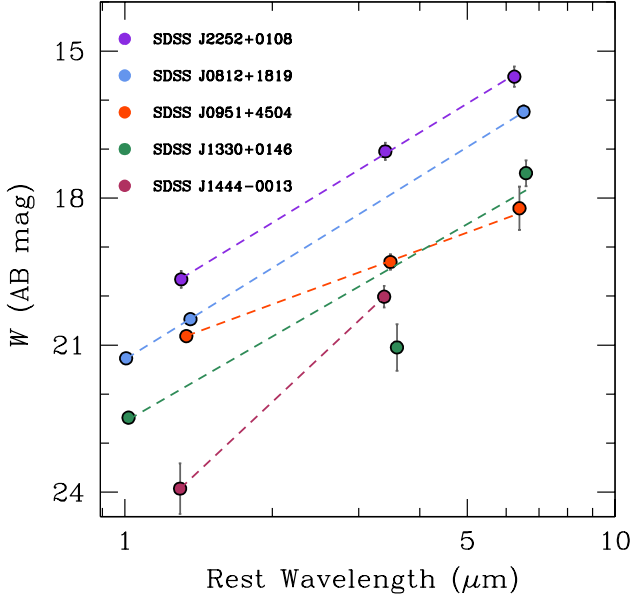


FIG. 5.— Example power-law fits to *WISE* photometry (AB mag). Each source is shown in a different color, with dotted lines showing our fits. Only three bands are fitted because we exclude those with rest wavelengths $< 1\mu\text{m}$. We use these power-law fits to find the luminosity at a rest wavelength of $3\mu\text{m}$. These objects span the range of *WISE* photometry quality in the sample.

There are four matches, one observed with APO, and the other three with Magellan. We used the filter transmission data from Hewett et al. (2006) to determine integrated fluxes from our APO and Magellan spectra. The APO target SDSS J222946.61+005540.5 (from now on we will abbreviate the SDSS names as SDSS J2229+0055) has a spectrophotometric H -band magnitude that agrees with the UKIDSS measurement to within 0.2 mag. Three objects observed with Magellan had matches in the UKIDSS survey. One (SDSS J1406+0429) has H and K -band magnitudes that agree within 0.2 magnitudes with the UKIDSS survey.

The analysis of the other two objects is more complicated. SDSS J0958+0135 was observed with COSMOS (Scoville et al. 2007) and so has additional data (Paper I). The UKIDSS magnitude of $H = 20.2$ mag (AB) agrees with the UKIRT value of $H = 20.0$ mag quoted in Paper I (Ilbert et al. 2009), but is two magnitudes brighter than our $H = 21.97$ mag. Such a large discrepancy is difficult to attribute to slit losses alone. We do detect line emission from this object, so it was at least partially in the slit. The apparent SED is quite red; it has SDSS $z = 21.9$ mag. In principle it is possible that the strange colors are caused by variability, and indeed our sources show striking similarities with the UV spectrum of NGC 5548 in the low state (Goad & Koratkar 1998). On the other hand, the UKIDSS and UKIRT photometry agree and were taken at different epochs.

Our final match, SDSS J1339+0441, observed with Magellan, is also considerably fainter in the spectral continuum than the imaging, with UKIDSS finding $H = 20.6$ mag as opposed to $H = 21.4$ mag from our FIRE spectrum. Again, the source is quite faint in the observed red, with SDSS $z = 21.1$ mag, but apparently brightens by a magnitude between the z and H bands. With so few points of comparison, it is difficult to diagnose the origin of these discrepancies. We are in the process of obtain-

ing NIR imaging for a larger sample. In the meantime, our flux calibration, particularly for the FIRE data, currently has at least a factor of two uncertainty.

4. LINE FITTING AND FLUX MEASUREMENTS

To obtain continuum flux and luminosity as well as emission line widths, fluxes and luminosities, we fit Gaussian+continuum models to the [O III], $H\alpha$, and [N II] lines (Table 2). The [O III] $\lambda\lambda 4959, 5007$ lines have low critical density, and thus unambiguously trace the kinematics in the low-density narrow-line region. We accordingly fit the [O III] lines first, fixing their relative wavelengths to laboratory values and their line ratio to 1:3. We allow up to two Gaussian components for this fit (following Greene & Ho 2005a), and simultaneously model the $H\beta$ line with the same shape. We minimize χ^2 using Levenberg-Marquardt minimization as implemented by MPFIT (Markwardt 2009). In most cases the $H\beta$ line is too weak to allow us to model a broad component. The exceptions are SDSS J1309+0205, where we detect a strong $H\alpha$ line and a broad component to $H\beta$, SDSS J1406+0429, where the $H\beta$ line is stronger than the [O III] line, and SDSS J1032+3736, where [O III] is not significantly detected. In these cases, $H\beta$ is allowed an additional broad Gaussian component, whose width is determined independently of $H\alpha$.

We derive uncertainties on all fit parameters using Monte Carlo simulations. We start with the best-fit model, and then create 500 artificial spectra by adding Gaussian random noise generated from the error spectrum. We fit each of these artificial spectra in an identical fashion, and the errors we quote enclose 68% of the artificially generated values. Errors on all parameters are derived in this manner.

We adopt the [O III] fits as a model for the narrow components of $H\alpha$ + [N II]. Again the relative wavelengths are fixed, as is a ratio of 1:3 for the [N II] $\lambda 6548$ /[N II] $\lambda 6584$ lines. Only the overall redshift and the flux scale of the narrow $H\alpha$ and [N II] lines, along with the local continuum, are free parameters. In the two cases where [O III] is undetected, we model the narrow-line region as a single Gaussian with σ allowed to vary. We then perform a second fit including a broad $H\alpha$ component as well, represented as a Gaussian with the same redshift to within 250 km s^{-1} . It is always challenging to determine whether or not a given line includes a broad component (e.g., Ho et al. 1997; Zakamska et al. 2003; Greene & Ho 2004; Hao et al. 2005; Reines et al. 2013). As above, we run Monte Carlo simulations to determine the errors in each parameter. We deem the broad component significant if $\chi^2_{\text{nobroad}} - \chi^2_{\text{broad}} > 4$ and the broad-line flux is detected at $> 3\sigma$ confidence. Note that we add only two free parameters, so this minimum increase in χ^2 should represent a significant improvement in the fit. In practice, the improvement is far larger than this in nearly all cases. Applying these two criteria, all but two of the 16 quasars that include $H\alpha$ in their bandpass require a separate broad $H\alpha$ component. The two exceptions are SDSS J1032+3735 and SDSS J2252+0106. In the case of SDSS J1032+3735, we do not detect the [O III] line significantly, so the decomposition is suspect. Neither object stands out in other regards. The line fits to the Magellan spectra are shown in Figure 2, to the APO spectra in Figure 3, and to the Gemini spectra in Figure 4.

4.1. CIV Fits

We then fit the C IV $\lambda\lambda 1548, 1551\text{\AA}$ lines from the SDSS spectra. We model the C IV line as a doublet, with a velocity

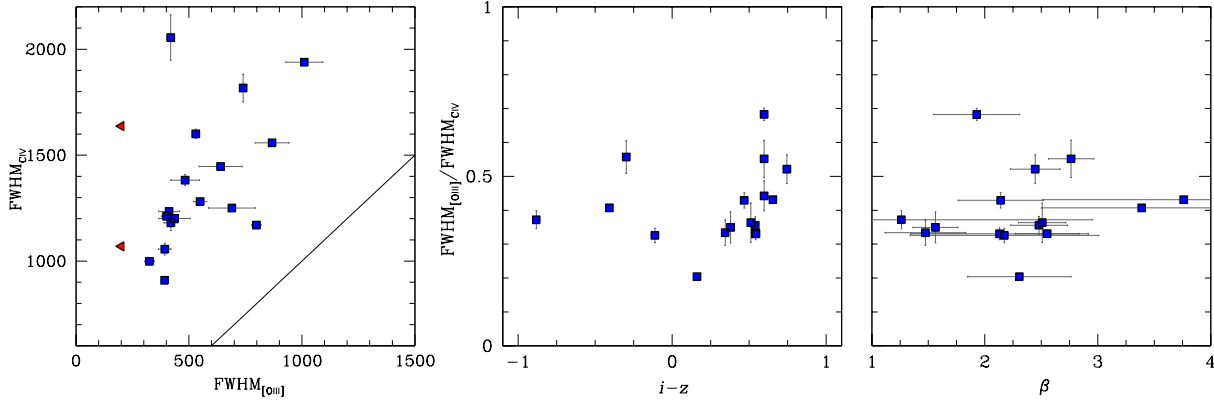


FIG. 6.— *Left*: Comparison of $\text{FWHM}_{\text{OIII}}$ and FWHM_{CIV} , as measured from the full profile fit to the broad and narrow components of C IV. The upper limits on [O III] (red triangles; SDSS J1032+3736 and SDSS J1342-0045) are simply assigned a FWHM of 200 km s^{-1} for illustrative purposes. The solid line demonstrates the 1:1 relation. *Middle and Right*: Ratio of FWHM_{CIV} to $\text{FWHM}_{\text{OIII}}$ as a function of rest-frame UV color ($i-z$) and the MIR spectral slope β that we fit to the four *WISE* bands (§4.2). Both SDSS J1406+0429 and SDSS J0906+0309 are missing from the right-hand panel, since they do not have sufficient *WISE* detections to measure a slope. We see no correlation between continuum color and the dominance of the broad line.

splitting of $\sim 500 \text{ km s}^{-1}$ fixed to the laboratory values, and a line ratio of 0.9:1 (red:blue) taken from NIST (Kramida et al. 2013)¹⁰. While this line ratio is most appropriate for the high densities and/or high line optical depths of the broad-line region, we do not have adequate S/N to independently constrain the narrow-line ratios (Hamann et al. 1995). Each component is modeled with the same line width, so we introduce no additional free parameters. As above, we assume that the [O III] line traces the kinematics of the narrow-line region, and constrain any narrow component of C IV to have that shape. We simultaneously allow the code to fit the residual flux with a single Gaussian for each member of the doublet, with relative wavelengths and line ratios fixed but all other components left as free parameters, only constraining the broad-line central velocity to fall within $\pm 250 \text{ km s}^{-1}$ of the narrow line. A serious complication arises from the prevalence of absorption on the blue side of the C IV line. We mask the absorption regions by hand, based on the asymmetry in the line profiles. The masked regions are indicated as dashed lines in Figures 2 and 3. Errors are derived via fits to simulated spectra as for H α and [O III].

We again use the difference in χ^2 of the two fits (with and without the broad component), combined with the S/N of the line, to decide whether the additional broad component is justified. Absorption causes additional challenges. For example, the C IV in SDSS J0812+1819 appears to have a broad base, but without the blue side of the line our detection is not very secure. In two cases, SDSS J1155+0444 and SDSS J1342-0045, we have only upper limits on a broad component. Below we will examine whether the relative strengths of the broad and narrow components depend on any interesting physical parameters of the system.

4.2. *WISE* Luminosities

One of the goals of this paper is to use broad-band SED information, including rest-frame optical and UV line luminosities and continuum measurements, to determine the intrinsic luminosities of our targets. Since the infrared emission from hot dust near the central AGN should be relatively isotropic (although see Nenkova et al. 2008; Liu et al. 2014), we consider the photometry from the Wide-Field Infrared Survey Explorer (*WISE*; Wright et al. 2010), which covers 3–26 μm . In Paper

I we cross-matched the SDSS target list with the *WISE* All-Sky Data Release. We found only a few dozen matches with $> 5\sigma$ detections in at least one band. In this work, we perform forced photometry of the *WISE* images at the positions of known SDSS sources (Lang et al., in prep). We convolve the *WISE* data with the point-spread function at the known positions of the SDSS sources. We then fit a model that includes a constant background level plus the point source to a small patch ($\sim 9 \times 9$ pixels, or $23 \times 23''$ for W1–W3 and twice that for W4) in the *WISE* images. The amplitude of the point-source component of the model is a measurement of the flux at that position in the *WISE* images (regardless of whether the source is detectable in the *WISE* images). The formal variance of our forced photometry is equal to the per-pixel variance of the image being photometered times the noise equivalent area of the profile; $\text{var}(f) = \sigma^2 / \sum_i p_i^2$ where p_i is the normalized profile (evaluated at pixel i) and σ^2 the per-pixel noise variance. We include in the fit all images available in the AllWISE data release.

Taking this forced photometry, we can examine the colors and luminosities of our sources in the MIR. We find that the median MIR color of the class A sources from Paper I is $\langle W1 - W2 \rangle = 1 \text{ mag}$ (Vega). As we showed in Paper I, the colors of our targets match those of the general BOSS quasar population at matching redshift and luminosity. In contrast, *WISE*-based AGN selection algorithms focus on the red end of our distribution, for instance $W1 - W2 > 0.8 \text{ mag}$ (e.g., Stern et al. 2012; Eisenhardt et al. 2012; Wu et al. 2012). Our targets are also 1–3 mag fainter in *WISE* than the Stern et al. sample.

Next, we measure the *WISE* luminosity at a fixed rest-frame wavelength. We select $3\mu\text{m}$ as the longest wavelength that allows inclusion of our highest redshift targets. To find the rest-frame $3\mu\text{m}$ luminosity, we fit all bands with a single power law for all rest wavelengths longer than $1\mu\text{m}$, where the quasar SED turns up due to hot dust. We have detections in three or more *WISE* bands longward of $1\mu\text{m}$ (rest) and do not carry out such fits in the few cases where we have a detection only in a single band. A simple power-law provides a fine description of the SEDs, which are all rising towards the red. We record both the rest-frame $3\mu\text{m}$ flux and the slope of the power-law β for use below (Fig. 5). In the future, we will leverage broad-band in-

¹⁰ <http://physics.nist.gov>

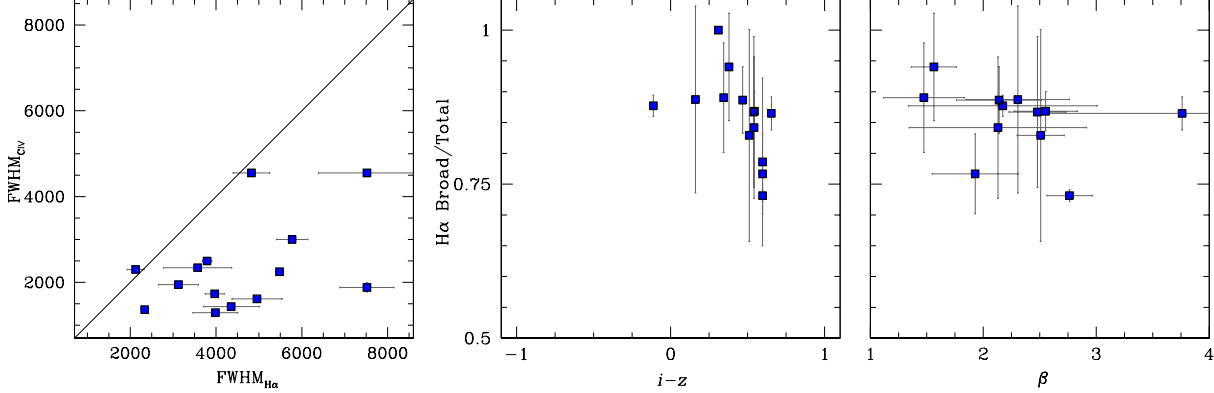


FIG. 7.— *Left*: Comparison of the broad component of the C IV line as measured from the multi-Gaussian fit with the broad component of H α . Solid line indicates the unity relation. We see no clear correlation between the two. The H α linewidths are systematically broader by factors of two or more. *Middle and Right*: Ratio of flux in broad H α to the total flux in the line as a function of rest-frame UV color ($i-z$; middle) and the MIR spectral slope β that we fit to the *WISE* bands (right). SDSS J1406+0429, SDSS J0906+0309, and SDSS J1342–0045 are missing from the right-hand panel, since they do not have sufficient *WISE* detections to measure a slope. We see no correlation between continuum color and the prominence of the broad line, similar to the case with C IV.

formation from GALEX to *WISE*, combined with sophisticated multi-component models to the SEDs following the technique of Lusso et al. (2013).

5. RESULTS

We now examine the rest-frame optical line widths and strengths in an attempt to understand in more detail the nature of our candidate Type II quasars. Qualitatively, the rest-frame optical emission line properties appear as we expect. We find high ratios of [O III] to H β in nearly all sources, in contrast to NLS1 galaxies that are characterized by [O III]/H β < 3 (e.g., Osterbrock & Pogge 1985). We detect broad components in the H α line that are systematically broader than those we see in C IV, while on average in the quasar population as a whole, C IV is broader, albeit with large scatter (e.g., Shen & Liu 2012). We only rarely detect broad H β , and will use this fact to place limits on the extinction of the broad-line region in §5.2.

In what follows, we will investigate the incidence of broad permitted lines, the broad-band SEDs, and the relationship between [O III] rest-frame EW and luminosity as clues to the nature of our quasars.

5.1. Line Widths and Shapes

We start with the incidence and properties of the broad permitted lines. In all cases we measure line widths from the Gaussian fits. For [O III], we measure the FWHM from the total fit to the line. For H α we quote the broad-line FWHM based on the Gaussian fit. In the case of C IV, we calculate both a *total* linewidth, measured nonparametrically on the combined narrow+broad line fit, for comparison with [O III], and a *broad* linewidth using just the single broad Gaussian, for comparison with H α . Recall that these targets were originally selected to have C IV line widths < 2000 km s^{−1} based on a single Gaussian fit with the width tied to other emission lines (excluding Ly α) performed by the SDSS pipeline (Bolton et al. 2012). The line widths that we present here make the physically motivated assumption that the [O III] linewidth traces the narrow-line region, while any additional component we find in the C IV lines arises from the broad-line region. Thus we are able to uncover weak broad emission not captured by the pipeline fit.

Narrow-line widths, as measured from the [O III] lines, range from 200 to 1000 km s^{−1}, consistent with lower-redshift narrow-line regions in luminous targets (Fig. 6, e.g., Hao et al. 2005; Reyes et al. 2008; Liu et al. 2013b). We detect significant broad H α in all of the targets, ranging in width from 1000 to 7500 km s^{−1}. Likewise, we detect an additional component beyond the [O III] model in every C IV line. The total C IV linewidths span only 1000 to 2000 km s^{−1} (Figures 2 & 3). The broad C IV linewidths range from 1300 to 4500 km s^{−1}, but nearly all have FWHM \lesssim 3000 km s^{−1}, and they are systematically lower than the broad component seen in H α (Figure 7, left).

We seek correlations between the broad-line widths and broad-line fractions with continuum color. First, in Figure 6, we compare the profile widths of [O III] (the bona-fide narrow-line region) and total linewidth of C IV. The two are strongly correlated, but the C IV line is \sim 2.5 times as broad as [O III] on average. We see no clear correlation between $\text{FWHM}_{[\text{O III}]}/\text{FWHM}_{\text{CIV}}$ and optical or mid-infrared color. We also search for a correlation in line shifts between [O III] and C IV, but found no correlation (Spearman rank $\rho = 0.15$, probability of no correlation $P = 0.5$).

To emphasize the narrowness of the broad component of C IV, we compare it with the broad H α (Figure 7, left). With a couple of exceptions, the H α lines are roughly twice as broad as C IV. The ratio of C IV to H α in typical blue quasars is known to span a large range (e.g., Greene et al. 2010; Assef et al. 2011; Shen & Liu 2012; Ho et al. 2012), but on average the C IV line is broader than H α in unobscured quasars. We also examine the ratio of broad to total flux in H α (Figure 7) and C IV (Figure 8). The broad component dominates the total line flux in both lines in most cases. There is no strong correlation between the broad-line fraction and mid-infrared color, perhaps because the latter spans such a narrow range.

Our targets were selected to have narrow C IV, but with physically motivated decompositions, we can state that there is a broad component distinct from [O III] and that it is relatively narrow. While most of our targets have broad linewidths \sim 2000 km s^{−1} (Figure 7), in the Shen et al. (2011) compilation of SDSS quasars, only 1% of $2 < z < 3$ quasars have C IV lines narrower than 2000 km s^{−1}. The fraction rises

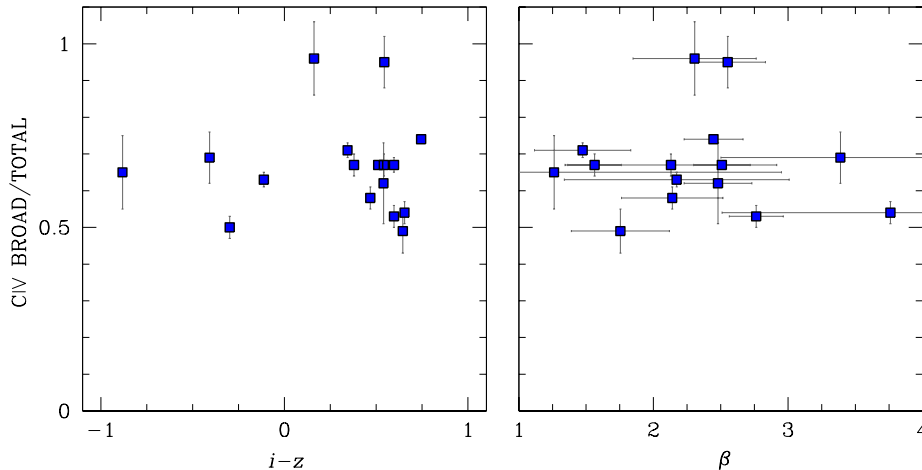


FIG. 8.— Ratio of broad to total flux in the C IV line, as a function of rest-frame UV (left) and MIR (right) color. The narrow-line profile is set by our [O III] fits. Broad C IV was detected in all cases. We see no correlation between line width ratios and optical or mid-IR color.

to 10% when we match in luminosity ($-23.5 < M_i < -25.5$ mag, with no extinction correction applied to either sample). In contrast, comparing the distribution of $H\alpha$ linewidths between our sample and the objects in the Shen et al. (2011) catalog with $-23.5 < M_i < -25.5$ mag, we find comparable median FWHM in $H\alpha$ of 4000 km s^{-1} and 3300 km s^{-1} , respectively. A Kolmogorov-Smirnov test suggests the two distributions are marginally consistent ($P = 0.06$), with our objects having broader lines on average. Thus, extinction is a natural culprit to explain the weakened broad emission lines at UV wavelengths, assuming a standard wavelength dependence for the reddening law. In the next section we will quantify the amount of extinction needed to explain our observations. We note that some of the absorption may arise from intervening (York et al. 2006) or associated absorbers (Vanden Berk et al. 2008).

To summarize this section, we detect permitted line emission that is broader than the narrow-line model alone. The broad C IV lines are relatively narrow (with FWHM ranging from 1000 to 4500 km s^{-1} , but most having $\text{FWHM} \approx 2000 \text{ km s}^{-1}$). These relatively narrow linewidths are not surprising, given the initial sample selection. In contrast, the $H\alpha$ lines span a more typical range of widths from 1000 to 7500 km s^{-1} . Let us now examine whether we can explain the difference between these two lines using extinction.

5.2. Equivalent Widths and Extinction Estimates

Another valuable clue to the nature of our sources comes from comparing the [O III] line rest-frame equivalent widths (EWs) and luminosities. We assume that the [O III] is extended relative to the broad-line region. Moving from unobscured to obscured sources, we would expect $L_{[\text{O III}]}$ to stay constant at a given bolometric luminosity while the continuum is obscured and grows fainter. As a result, obscured sources should have much higher EWs at a given line luminosity (see Figure 9). The observed range of the [O III] $\lambda 5007\text{\AA}$ line EW is bracketed by obscured quasars at $0.5 < z < 0.8$ from Zakamska et al. (2003) and unobscured quasars at comparable redshift from Shen et al. (2011). Our targets lie between the obscured and unobscured sources.

We can derive an estimate for the extinction using the ratio of the observed rest-frame EW to that expected for an unobscured quasar with the same $L_{[\text{O III}]}$. Since we expect the [O III] flux to emerge from larger scales with lower extinction, the ratio of the observed and expected EW simply diagnoses the extinction level of the continuum at 5007\AA . Assuming SMC-like dust (Pei 1992), which appears appropriate for quasars (Hopkins et al. 2004), we calculate the extinction in the B -band, A_B , for the seven quasars with $\text{EW} > \text{EW}_{\text{unobscured}}$ and an $H\alpha$ measurement. Note that this estimate is independent of the absolute flux calibration. Based on this calculation, we find values of A_B ranging from 0.07 to 2.8 mags with a median of $A_B = 1.2$ mag (Table 3; $0.05 < A_V < 2.2$ mag; median $A_V = 0.9$ mag). For reference, a value of $A_B = 1.2$ mag corresponds to a transmitted UV flux at 1500\AA that is 14% of the intrinsic flux, assuming the SMC reddening curve of Pei (1992). The two largest extinction values belong to SDSS J1330+0146 and SDSS J0958+0135 (the latter is in COSMOS; Scoville et al. 2007, Paper I).

Given that in general we detect broad $H\alpha$ but not broad $H\beta$, we can derive a second estimate of the reddening A_B if we make the assumption that all objects have the same intrinsic $H\beta/H\alpha$ ratio. We derive 3σ limits to the broad $H\beta$ flux by integrating the $H\beta$ fit residuals over twice the FWHM of the $H\alpha$ line. We then estimate a lower limit to the extinction, assuming an intrinsic Case B' $H\alpha/H\beta$ ratio of 3:1. This ratio is reasonable, since the typical observed $H\alpha/H\beta$ ratio in lower redshift SDSS quasars is 4 : 1 (Greene & Ho 2005b).

Going a step further, we predict the broad C IV flux based on the observed broad $H\alpha$ flux and the calculated extinction. We assume that intrinsically the C IV line is 35% brighter than the $H\alpha$ line, based on the compilation of Shen & Liu (2012) of 60 SDSS quasars with $1.5 < z < 2.2$. We will use this single value although there is nearly an order of magnitude scatter in the ratio¹¹. The expected broad C IV flux is nearly always higher than what is observed by a factor of two to ten (with measurement errors causing a factor of ~ 2.5 uncertainties on these ratios). The one exception is SDSS J1330+0146, where the expected flux is only 6% of what is observed, but the broad emission lines are both quite weak in this case. There are two possible interpretations. Given that the broad component of C IV is much

¹¹ Our observed CIV/ $H\alpha$ ratios range from 0.04 to 2. We find no significant correlation between the observed line ratios and the reddening, but the total number of objects is small.

Table 2. Emission Line Properties

QSO (1)	$f_{[\text{O III}]}$ (2)	$\log(L_{[\text{O III}]})$ (3)	$\text{FW}_{[\text{O III}]}$ (4)	$f_{\text{C IV}}$ (5)	$\log(L_{\text{C IV}})$ (6)	$\text{FW}_{\text{C IV}}$ (7)	B/T (8)	$f_{\text{H}\alpha, \text{b}}$ (9)	$r_{\text{H}\beta}$ (10)	$r_{\text{H}\beta}$ (11)	$f_{\text{H}\alpha, \text{t}}$ (12)	$\log(L_{\text{H}\alpha, \text{t}})$ (13)	$\text{FW}_{\text{H}\alpha}$ (14)
J0220-0124	11.3±1.73	43.79±0.06	440±70	19.7±0.4	44.03±0.01	1200±60	0.72±0.06	7.72±1.4	<0.32	<0.56	37.4±5.9	44.36±0.11	3570±590
J0736+2259	6.35±0.88	43.39±0.06	480±70	8.40±0.4	43.52±0.02	1380±70	0.72±0.08	3.01±0.4	0.34±0.21	<0.88	47.3±3.1	44.32±0.08	5770±2170
J0738+4240	640±100	1450±70	0.72±0.07	...	0.13±0.05	3120±470
J0812+1819	76.1±5.61	44.53±0.03	420±40	2.20±0.2	43.00±0.04	1180±60	0.67±0.16	25.4±3.6	<0.25	<0.48	166±17.	44.91±0.09	3990±620
J0913+0342*	7.38±0.52	43.76±0.03	390±40	3.20±0.2	43.41±0.03	1160±60	0.79±0.18
J0951+4504	11.6±1.32	43.74±0.05	410±50	21.4±0.7	44.01±0.01	1230±60	0.76±0.07	5.51±1.2	<0.36	<0.63	44.7±3.2	44.37±0.08	2130±1030
J0958+0135*	8.66±0.12	43.84±0.01	740±70	10.1±0.9	43.91±0.04	1690±80	0.74±0.11
J1032+3736	<4.2	<43.0	840±410	8.70±0.5	43.57±0.03	1640±80	0.54±0.11	10.9±1.8	0.22±0.18	<0.89	10.9±2.2	43.72±0.13	...
J1155+0444*	3.00±0.09	43.14±0.01	800±80	7.80±1.2	43.56±0.06	1250±60	<0.30	2.85±0.1	0.63±0.11	0.38±0.07	9.36±0.6	43.68±0.08	4830±1050
J1309+0205*	8.44±0.46	43.50±0.02	330±30	8.40±0.1	43.50±0.01	1190±60	0.73±0.07	3.96±0.2	0.41±0.07	0.14±0.07	28.3±1.4	44.08±0.06	5480±520
J1330+0146*	1.49±0.07	42.80±0.02	420±40	4.30±0.6	43.27±0.06	990±50	0.67±0.11	0.47±0.05	0.11±0.14	1.02±0.16	3.70±0.4	43.25±0.10	7520±560
J1339+0441*	4.46±0.05	43.38±0.01	530±50	6.80±0.2	43.57±0.01	1460±70	0.79±0.11	2.61±0.2	<0.17	0.28±0.06	17.2±0.8	44.02±0.06	2340±1120
J1342-0045	3840±380	1070±50	<1.16	7520±1130
J1406+0429*	1.56±0.08	43.21±0.02	870±90	7.90±0.2	43.92±0.01	1580±80	0.59±0.08
J1444-0013*	4.97±0.04	43.41±0.00	390±40	3.90±0.1	43.31±0.02	990±50	0.62±0.08	4.09±0.2	0.11±0.08	0.11±0.05	26.1±1.3	44.18±0.06	3790±570
J1609+1905	690±100	1250±60	0.58±0.08	...	0.20±0.06	4350±650
J2153+0411	12.2±0.60	43.75±0.02	400±40	8.80±0.2	43.61±0.01	1210±60	0.72±0.08	5.21±0.4	0.30±0.13	<0.39	27.7±2.8	44.15±0.09	4960±520
J2229+0055	13.4±0.73	43.77±0.02	550±50	8.60±0.2	43.58±0.01	1280±60	0.63±0.08	5.77±0.5	0.11±0.13	<0.58	45.0±2.2	44.34±0.07	3970±1060
J2252+0108	28.7±2.46	44.17±0.04	1010±100	71.4±0.3	44.56±0.01	1940±100	0.79±0.06	39.7±19.	0.77±0.2	0.21±0.09	39.7±6.2	44.36±0.11	...

Note. — Col. (1): Quasar. Asterisk marks Magellan objects, for which flux calibration is less secure. Col. (2): Observed flux in the [O III] line (10^{16} erg s^{-1} cm^{-2}). Throughout, limits are 3σ . Col. (3): Log of the luminosity in [O III] (erg s^{-1}). Col. (4): FWHM of [O III] (km s^{-1}), measured from our two-Gaussian fit. Col. (5): Observed total flux in the C IV line (10^{16} erg s^{-1} cm^{-2}). Col. (6): Log of the luminosity in C IV (erg s^{-1}). Col. (7): FWHM of C IV (km s^{-1}), measured from the multi-Gaussian fit with the narrow component fixed to the [O III] model. Col. (8): Ratio of C IV flux in broad to total emission. Col. (9): Observed flux in the narrow H α line (10^{16} erg s^{-1} cm^{-2}). Col. (10): Ratio of [N II] λ 6584/H α_{narrow} . Col. (11): Ratio of H β /H α_{narrow} . Col. (12): Observed total flux in the H α line based on the multi-Gaussian fit (10^{16} erg s^{-1} cm^{-2}). Col. (13): Log of the total luminosity in H α (erg s^{-1}). Col. (14): FWHM of the broad H α component, when detected (km s^{-1}).

narrower than that of H α , one possibility is that we are not detecting the full broad C IV line, and that the actual extinction is greater than what we estimate from the Balmer decrement. Alternatively, the extinction curve may be flatter in the UV than the SMC curve (e.g., Gaskell et al. 2004), in which case we would be overpredicting the intrinsic C IV luminosity by factors of several. A third possibility is that the C IV/H α ratios are anomalous in these objects.

We compare the EW estimate for A_B with the limits derived from the flux ratio of H β /H α in Figure 10 (left). A value of $A_B = 0$ on the x-axis means that the [O III] EW is consistent with the unobscured quasars. The two estimates are correlated, which is encouraging, since both are estimates of the reddening to the continuum/broad-line region. In general, the H β -based absorption estimates are larger, perhaps because the underlying H β to H α ratios span a wide range, rather than having the Case B' recombination value (e.g., MacAlpine 1985; Rix et al. 1990; Korista & Goad 2004; Greene & Ho 2005b). The other possibility is that the [O III]-derived values are too low, because we have ignored extinction of the [O III] line and/or scattered light boosting the continuum emission in the Type II quasars. As a sanity check, we can also calculate the minimum extinction needed to bring the $r-W1$ color in line with the Richards et al. (2006) blue quasar SED. We find this minimum to be $A_B < 0.5$ mag ($A_V < 0.4$ mag) in all cases, consistent with the other estimates but less restrictive (Figure 10, right). We do not calculate the extinction using the narrow H β and H α lines because of the low significance of the H β detections.

In summary, based on the EW of [O III] and limits on the Balmer decrement in the broad emission lines, we find evidence for modest absorption ($A_B \approx 0-3$ mag or $A_V \approx 0-2.2$ mag).

5.3. Luminosity Indicators

We now investigate the SEDs and bolometric luminosities of these quasars. In a future paper we will present full SEDs, but for the moment we simply compare rest-frame UV and optical line luminosities with UV and mid-infrared continuum luminosities. In the case of unobscured sources, the rest-frame UV light traces the big blue bump directly, while the near to mid-

infrared emission (longward of ~ 1 μm) traces hot dust sitting close to the accreting black hole.

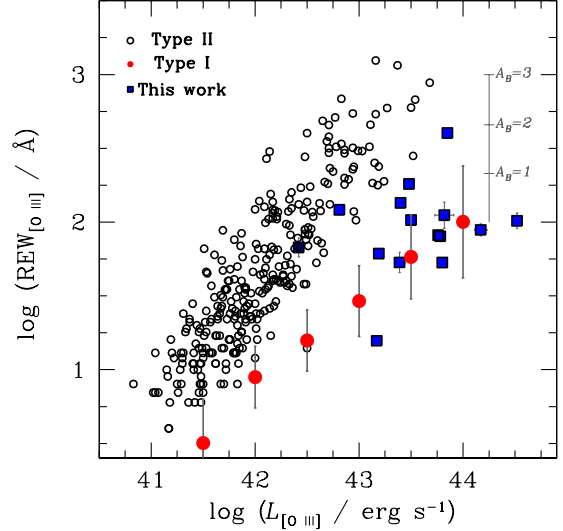


FIG. 9.— The rest-frame equivalent width (EW) of [O III] compared with the luminosity in the same line. The blue squares are the high-redshift obscured quasar candidates presented here. The open black circles are Type II quasars at lower redshift from Zakamska et al. (2003), while the red circles are median values from the Shen et al. (2011) catalog of Type I objects with $0.5 < z < 0.8$ to roughly match the Zakamska sample. Our objects are intermediate in properties between the obscured and unobscured sources. The extinction needed to make the [O III] EWs commensurate with the Type I objects' A_B is between 0 and 3 mag, as shown schematically with the grey bar. Two points are missing here, SDSS J0951+4504, where we only marginally detect the continuum, and SDSS J1032+3736, where we do not detect the [O III] line.

The latter, therefore, is expected to be relatively isotropic (although see also Nenkova et al. 2008; Liu et al. 2014). Line luminosities, in so far as they are photoionized by the central source, also correlate with the continuum luminosity (e.g., Yee 1980; Zakamska et al. 2003; Heckman et al. 2004; Greene & Ho 2005b; Liu et al. 2009). The narrow line luminosities should also be relatively isotropic (although see also Netzer et al. 2005). We compare various intrinsic luminosity indica-

tors with each other in Figure 11. In the case of H α and C IV, we plot total (broad+narrow) luminosities. We do this for consistency with other work (Greene & Ho 2005b), but since the narrow emission is such a small fraction of the total flux, removing it would make little difference to the final outcome.

Table 3. Black Hole Masses and Extinction Estimates

Quasar (1)	M_{BH} (2)	$f_{3\mu\text{m}}$ (3)	$\log(L_{3\mu\text{m}})$ (4)	$\log(L_{\text{UV}})$ (5)	$A_{B,B}$ (6)	$A_{B,O}$ (7)
J0220-0124	8.8	1140 \pm 220	45.8 \pm 0.07	45.71 \pm 0.01	0.1 \pm 0.2	0.1 \pm 0.3
J0736+2259	9.2	1180 \pm 280	45.6 \pm 0.09	45.41 \pm 0.01	0.3 \pm 0.2	< 0.3
J0786+4240	...	4930 \pm 1300	45.3 \pm 0.1	44.92 \pm 0.02
J0812+1819	9.2	1680 \pm 330	45.8 \pm 0.08	45.06 \pm 0.01	0.0 \pm 0.2	< 0.3
J0913+0342	...	<1650	45.6 \pm 0.32	45.01 \pm 0.07	...	< 0.3
J0951+4504	8.3	560 \pm 200	45.4 \pm 0.13	45.55 \pm 0.01	0.3 \pm 0.2	< 0.3
J0958+0135	...	<1140	45.4 \pm 0.28	45.54 \pm 0.01	...	1.6 \pm 0.1
J1032+3736	...	<1200	45.2 \pm 0.20	45.15 \pm 0.01	...	< 0.3
J1155+0444	8.7	820 \pm 260	45.5 \pm 0.12	45.18 \pm 0.01	1.1 \pm 0.3	0.8 \pm 0.1
J1309+0205	9.0	700 \pm 240	45.4 \pm 0.13	45.07 \pm 0.03	2.5 \pm 0.2	0.6 \pm 0.0
J1330+0146	8.9	<1290	45.2 \pm 0.24	44.92 \pm 0.03	0.0 \pm 0.4	2.4 \pm 0.1
J1339+0441	8.3	1200 \pm 220	45.8 \pm 0.07	45.31 \pm 0.01	3.0 \pm 0.2	1.2 \pm 0.0
J1342-0045	...	12300 \pm 2100	45.8 \pm 0.1	44.87 \pm 0.05
J1406+0429	...	<1560	46.3 \pm 0.00	45.75 \pm 0.01	...	< 0.3
J1444-0013	8.8	<690	45.0 \pm 0.32	44.92 \pm 0.03	2.7 \pm 0.2	1.6 \pm 0.0
J1609+1905	45.53 \pm 0.01
J2153+0411	9.0	<1320	45.3 \pm 0.21	45.49 \pm 0.01	0.2 \pm 0.2	< 0.3
J2229+0055	8.9	1380 \pm 450	45.7 \pm 0.12	45.35 \pm 0.01	0.5 \pm 0.2	< 0.3
J2252+0108	...	3890 \pm 1270	46.3 \pm 0.12	45.92 \pm 0.04	...	< 0.3

Note. — Col. (1): Quasar. Col. (2): Log of the black hole mass (M_{\odot}) as estimated from the broad line width in Col. (14) of Table 2 and the H α luminosity in Col. (12) of Table 2. Col. (3): Flux (λ_{f}) at rest-frame $3\mu\text{m}$ ($10^{-16}\text{erg s}^{-1}\text{cm}^{-2}$). Col. (4): Log of the luminosity at $3\mu\text{m}$ (erg s^{-1}). Col. (5): Log of the luminosity at 1500\AA (erg s^{-1}). Col. (6): Extinction at B -band (mag) from the Balmer decrement. Col. (7): Extinction at B -band (mag) from the [OIII] EW.

If there is substantial extinction of the broad-line region specifically, then we expect the weakest correlation between the strength of the C IV line and the UV continuum emission, while correlations with progressively redder diagnostics should be stronger. The tightest correlation is expected to be between the *WISE* and [O III] luminosities, as the most isotropic.

In fact, we do not find significant correlations between any of our luminosity probes (Figure 11), based on Spearman rank coefficients. We have also investigated $L_{\text{H}\alpha}$ and $L_{[\text{OIII}]}$ against the UV luminosity, and find no significant correlation. We also show the “dereddened” UV and C IV fluxes, adopting the Balmer decrement estimates of A_{λ} ; even with an extinction correction, we detect no correlation. In general the luminosity indicators all span a similar range of ~ 2 dex. The one exception is the observed UV luminosity, which spans a narrow range. Considering that we selected the targets to be at the flux limit of the BOSS survey and to have high-EW emission lines, the narrow observed range in UV luminosity may be no more than a selection effect.

There are two possible explanations for the lack of luminosity correlations. One is the limited range in observed luminosity of the sample. It may be that intrinsic SED differences, combined with extinction of the narrow-line region, wash out correlations over the narrow luminosity range we probe here. Bona fide Type II quasars at $z \sim 0.5$ are clearly redder in the MIR than are unobscured quasars, possibly adding additional scatter to the *WISE* luminosities (e.g., Liu et al. 2013b). The other major caveat here remains outstanding uncertainties in our flux calibration. We have tried splitting the data into APO and Magellan subsamples to see if a strong correlation holds with one or the other, but the total number of objects is too small to seriously address this question.

5.4. Black Hole Masses

With rest-frame optical spectra, and detected broad emission lines, we can use scaling relations to estimate black hole (BH) masses for these luminous quasars (e.g., Vestergaard 2002; Shen et al. 2008; Kelly et al. 2009). We assume that only gravity influences the motions of the broad-line region gas, so that the velocity dispersion of the gas relates directly to M_{BH} ; $M_{\text{BH}} \propto Rv^2$. We also need a size scale for the emitting gas, which we estimate from the AGN luminosity using the “radius-luminosity” relation, calibrated using radius measurements from reverberation mapping (e.g., Kaspi et al. 2000; Bentz et al. 2009, 2013). Because we do not detect the optical AGN continuum directly in our observations, we rely on the known correlation between continuum and line luminosity (e.g., Yee 1980) to calculate the BH mass from observations of the H α line alone (uncorrected for extinction). The relationship between continuum luminosity and line luminosity, as well as the relation between H β and H α FWHM, are taken from Greene & Ho (2005b), while the radius-luminosity relation is taken from Bentz et al. (2013).

BH masses derived in this manner clearly carry a large number of systematic uncertainties that are difficult to quantify (e.g., Krolik 2001; Greene & Ho 2006). Including these systematics, the BH mass uncertainties are estimated to be factors of a few (e.g., Vestergaard & Peterson 2006; Shen 2013). Eventually we hope two-dimensional reverberation mapping of nearby Seyfert galaxies will mitigate these problems (e.g., Bentz et al. 2008; Denney et al. 2010; Barth et al. 2011; Pancoast et al. 2012; Kashi et al. 2013), but in the meantime we must be careful not to overinterpret the BH mass estimates.

Taking the measurements at face value, the derived BH masses are typically $\sim 10^9 M_{\odot}$. Technically, these are lower-limits, since they rely on the H α luminosity, which almost certainly suffers extinction. On the other hand, the inferred M_{BH} only depends on the square root of the H α luminosity; a factor of three error in broad H α luminosity corresponds to only a 0.24 dex change in M_{BH} . The line width may be underestimated due to extinction as well, but given that the distribution of H α widths spans a similar range to other quasar samples (e.g., Greene & Ho 2007; Shen & Liu 2012; Banerji et al. 2012; Matsuoka et al. 2013; Banerji et al. 2013), it is hard to estimate how large that bias may be. For comparison, we show both the median source from the SDSS sample in a matching redshift and magnitude range (Shen et al. 2011) as well as the median object from a NIR-selected sample presented in Banerji et al. (2012).

We can ask whether these masses are reasonable given the total luminosities of the objects. In addition to factors of a few uncertainties in M_{BH} , there are also a number of uncertainties involved in calculating the bolometric luminosities. The composite SED of unobscured objects in Richards et al. (2006) shows that the bolometric luminosity is 7–10 times $L_{3\mu\text{m}}$. Using this scaling, the majority of the sample has sensible Eddington ratio estimates of $\sim 10\%$, with all targets consistent with being below the Eddington limit. Considering the lack of correlation between *WISE* and [O III] luminosities discussed above, these Eddington ratios are no better than order-of-magnitude estimates. The largest uncertainty is in our choice of the broad emission line used to measure the gas velocity dispersion. If we used the C IV linewidth instead of the H α linewidth, our M_{BH} values would be ~ 4 times smaller on average. However, there may be a component of the C IV that is completely obscured. Thus the H α linewidth may be more representative of the broad-line

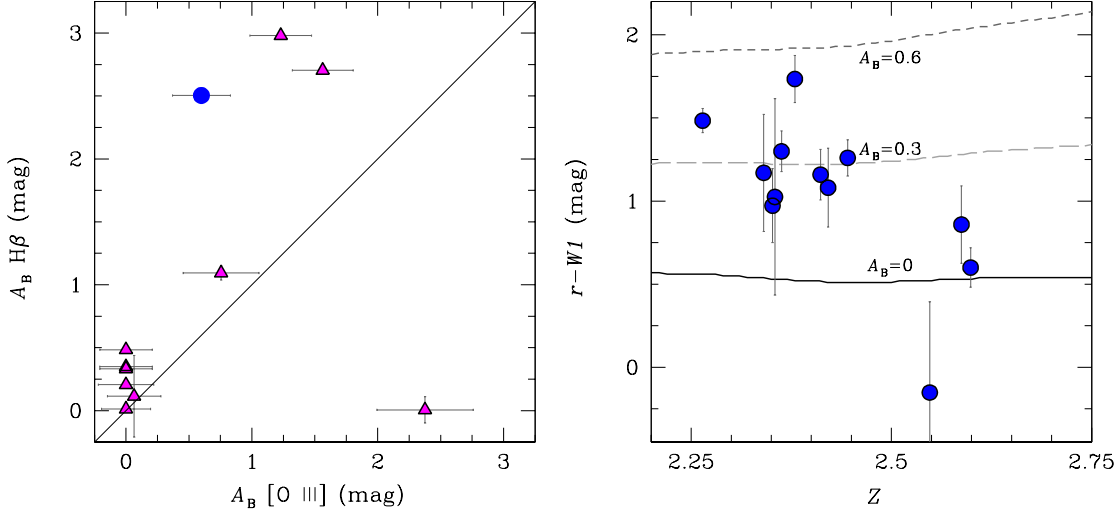


FIG. 10.— *Left:* We compare two estimates for A_B (mag). The first is derived by assuming that any positive deviations from the average [O III] EW are caused by extinction of the continuum. The second takes limits on the broad H β flux and assumes an intrinsic H α /H β ratio of 3.01:1. The latter estimate is a lower limit on A_B , to the extent that the assumption of Case B' ratio is correct. The blue symbol is SDSS J1309+0205, for which we detect a broad H β component. The solid line indicates the 1:1 relation. *Right:* The observed $r-W1$ color as a function of redshift, plotted against the color of the Richards et al. (2006) SED with absorption ranging from $A_B = 0$ to $A_B = 0.6$ mag, showing that only moderate extinction is required to explain the observed UV to NIR colors.

region kinematics.

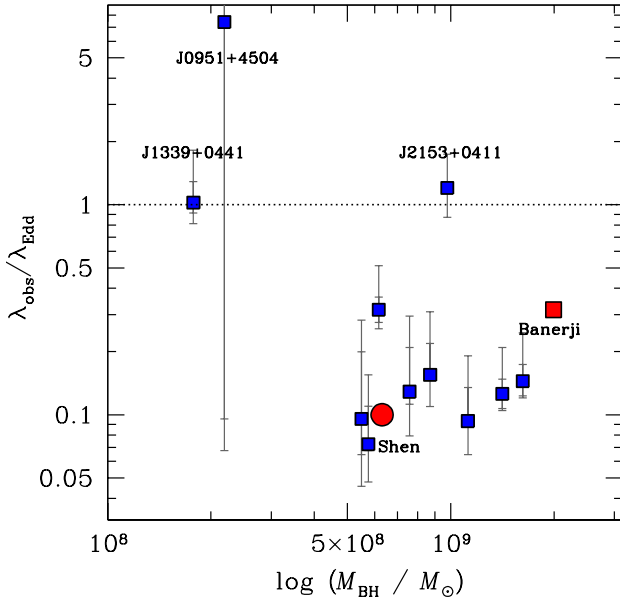


FIG. 12.— BH masses compared with the ratio of bolometric to Eddington luminosity, λ . We estimate BH masses based on the H α FWHM and the H α luminosity (Greene & Ho 2005b). The bolometric luminosities are derived from $L_{3\mu\text{m}}$, and the uncertainties reflect both random errors (in H α luminosity and FWHM) and systematic errors in bolometric corrections, as indicated by the double error bar. Systems with very large error bars have very uncertain broad H α FWHM. We have *not* incorporated systematic uncertainties in the BH masses here. Without that uncertainty, we can already see that the majority of the targets do not violate the Eddington limit ($\lambda = 1$). For comparison, we show the median M_{BH} and λ for the optically selected sample of Shen et al. (2011) in a matching redshift and magnitude range (big red circle), as well as the median M_{BH} and λ for the NIR-selected sample of Banerji et al. (2012).

5.5. Multi-peaked Objects

Paper I highlighted an intriguing sub-sample of our targets that contained multiple velocity peaks in their C IV spectra. We postulated that, since C IV is a resonance line, absorption was the most likely explanation for the subcomponents, rather than physically distinct clumps of gas with differing kinematics. We specifically obtained NIR spectra for two of these sources (SDSS J1339+0441 and SDSS J1444-0013, the latter subsequently fell out of the main sample in Paper I due to revised C IV line width measurements). Here we compare the C IV and [O III] line profiles (Figure 13).

In Figure 14 we show the two-dimensional, flat-fielded and sky-subtracted FIRE spectrum of SDSS J1339+0441, which clearly has a multi-peaked structure in both the 4959 and 5007 lines. We also see strong sky residuals directly to the red of [O III] $\lambda 5007$. In SDSS J1339+0441 the [O III] line has a complicated velocity structure with multiple kinematic components, although less distinct than that in C IV. This profile could be due to outflow kinematics (Greene & Ho 2005a; Greene et al. 2011; Liu et al. 2013a,b) or to narrow line regions around distinct black holes (e.g., Djorgovski et al. 2007; Barth et al. 2008; Comerford et al. 2009; Liu et al. 2010, 2011), as found in low-redshift objects. Another intriguing possibility specific to high-redshift objects is that the quasar host galaxy is being formed from multiple components which are illuminated by the main quasar (e.g., Elmegreen et al. 2008; Förster Schreiber et al. 2011).

We now directly compare the velocity structure in the C IV and [O III] lines. Since C IV is a doublet, it is tricky to perform a direct comparison of the two lines (Hainline et al. 2011). As throughout the paper, we assume that the [O III] provides a model for the narrow-line region. We then assume the same redshift for both the [O III] and C IV lines, and construct a model

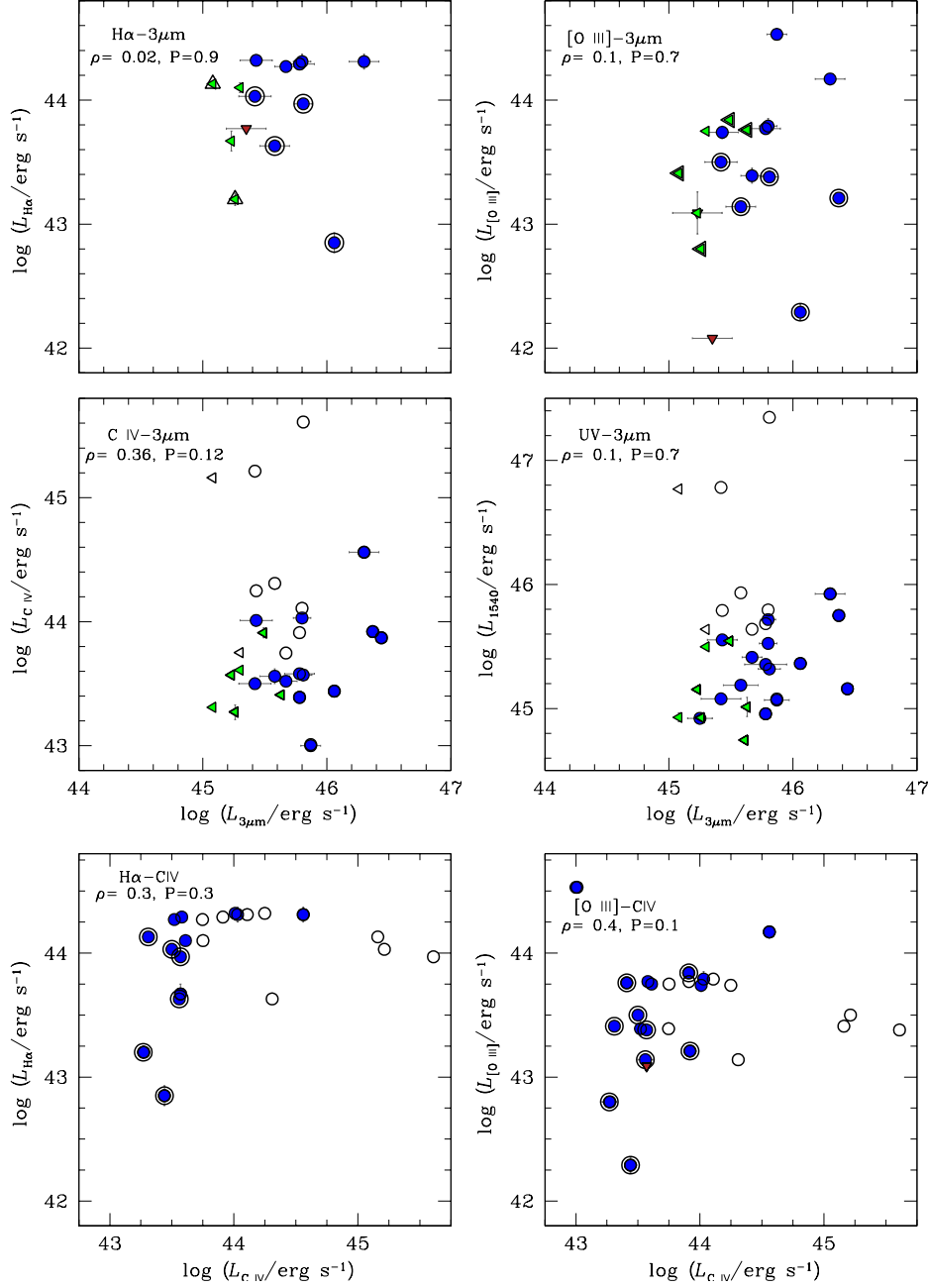


FIG. 11.— Comparison of various luminosity indicators, all in units of erg s^{-1} . The bottom two panels compare the line luminosity of C IV with total H α (left) and [O III] (right). Magellan targets are indicated with double symbols; we see that while we preferentially targeted sources with lower rest-frame optical-UV luminosities with Magellan, these targets alone are not responsible for the observed scatter. In the top four panels, we compare with the *WISE* luminosity at a rest-frame wavelength of $3\mu\text{m}$. Errors are plotted on all points, but are often comparable to the symbol size. The y-axis 3σ upper limits are plotted as downward red arrows, while the x-axis 3σ upper limits are plotted as green rightward pointing arrows. The dereddened values are shown as open symbols and are based on the Balmer decrement limits from the non-detection of broad H β lines. There are no strong correlations between any of these indicators, although in general they cover comparable ranges in luminosity. The one exception is the narrow range of the UV continuum luminosity, perhaps just reflecting our UV selection.

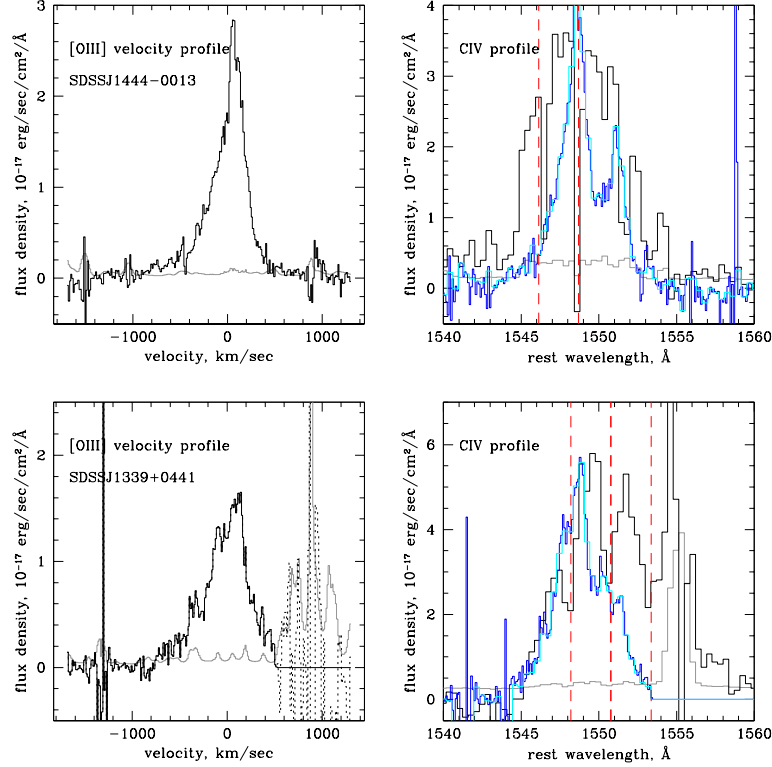


FIG. 13.— The [O III] $\lambda 5007$ and C IV profiles for two objects with multiple C IV velocity peaks. We attempt to model the C IV doublet using the velocity profile of the [O III] line. On the left we show the [O III] line, while on the right we superpose the [O III] model on the C IV spectrum, with the two components fixed to the wavelengths of the doublet and a line ratio of 1:2 (Hamann et al. 1995), although we tried 0.9:1 as above and it did not change the results. We present the Magellan spectrum (dark blue), the Magellan spectrum smoothed to BOSS resolution (light blue), and the error array (grey). Differing spectral resolution alone cannot explain the observed discrepancy in line shape. In the lower left panel, the high noise immediately to the red of the [O III] line in SDSS J1339+0441 shown with the dotted line is due to atmospheric emission residuals. We mask this part of the [O III] velocity profile in our model of the C IV profile. Although velocity structure is clearly visible in the [O III] line for SDSS J1339+0441, we cannot fully explain the C IV profile in either source. For example, the C IV emission is both broader and more complex than the [O III] emission in both cases. Furthermore, there is an apparent additional absorption system in both cases (red dotted lines), but these putative absorption systems would be very narrow, and do not have the proper line ratios between the two C IV components.

C IV profile as the superposition of two lines with the same line shape in velocity space as the [O III] line. We convert the FIRE spectra to vacuum wavelengths, place the two doublet components at their laboratory wavelengths, and impose a line ratio of 1:2 (Hamann et al. 1995) (although we also tried 0.9:1 as above; the results do not change).

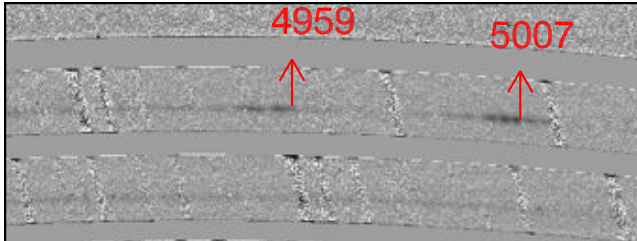


FIG. 14.— Flat-fielded and sky-subtracted two-dimensional spectrum for the quasar SDSS J1339+0441, which has multiple clumps in the [O III] line shown here. The grey bands represent gaps between orders, and the galaxy continuum is clearly visible in both orders shown here. The arrows roughly indicate zero velocity for the 4959 (left) and 5007 (right) lines. The clumps are $\sim 300 \text{ km s}^{-1}$ apart, are far from strong sky lines, and are most likely intrinsic.

Much like all other targets studied in this paper, the C IV line in both triple-peaked objects has a broad base that cannot be explained by a simple superposition of the [O III] lines (Figure 13). Furthermore, some narrow absorption must be superposed on the C IV emission profiles to fully explain their velocity structure. We indicate in dotted red lines the locations of these putative absorbers in each system. However, this additional absorption is only marginally broader than one pixel, making it quite suspect, and the doublet line ratios are not sensible.

In summary, these multi-peaked objects have become more intriguing and more mysterious with our additional NIR data. On the one hand, in one case we found velocity structure in the [O III] line, which, unlike in the C IV, cannot be due to blue-shifted absorption. On the other hand, we cannot fully explain the observed C IV kinematics with a simple superposition of the [O III] line profiles. We either must postulate absorption in addition to real velocity structure, or accept that the line shapes are unrelated. For instance, perhaps the C IV arises from the broad-line region, or an intermediate-line region sitting between the classic narrow and broad-line regions (Brotherton et al. 1994).

6. DISCUSSION AND SUMMARY

We started with a sample of Type II quasar candidates selected from BOSS, with relatively narrow and high-EW C IV emission lines. In this paper we present NIR spectroscopy in the *JHK* bands, covering $H\beta$ and [O III] emission in all cases, and $H\alpha$ in most. Our primary motivation is to investigate the nature of these targets, specifically whether they are in fact obscured quasars. Overall, our analysis points to a population of moderately obscured ($A_B \sim 0-3 \text{ mag}$) quasars powered by $\sim 10^9 M_\odot$ BHs radiating at a healthy $\sim 10\%$ of their Eddington limits.

From Paper I, we know that our quasar targets have UV luminosities that are too high to be described by star formation alone. On the other hand, we did detect polarization at the level of $\sim 3\%$ in the two observed targets (Paper I), larger than the 0.5% typical of unobscured quasars (Berriman et al. 1990). Furthermore, we see evidence that the UV luminosities are somewhat suppressed, in the broad-band SED of SDSS J0958+0135

presented in Paper I and also in the low ratio of UV to *WISE* luminosity (Figure 11). Thus, the continuum measurements support a moderate-obscuration scenario.

We use multiple techniques to estimate the level of extinction. The narrow-line equivalent widths point to modest extinction; in general [O III] has higher EW than a typical unobscured quasar, but not as high as the locus of Type II quasars at $z \approx 0.5$ (Zakamska et al. 2003). Turning the observed EW discrepancy into an estimate of the extinction produces $0 < A_B < 3 \text{ mag}$ or $A_V \approx 0-2.2 \text{ mag}$. Based on this A_B , the intrinsic UV luminosities would be boosted by $0.5-1 \text{ dex}$.

We also estimate the extinction using the non-detection of broad $H\beta$, and find rough agreement with the reddening estimates based on [O III] EW. The broad permitted line widths are also consistent with a moderate-obscuration scenario. Specifically, we detect significant broad emission lines in $H\alpha$ with line widths ranging from 1000 to 7500 km s^{-1} . In the UV, on the other hand, the C IV line fluxes are fainter than expected based on $H\alpha$ (assuming an SMC extinction law), and show considerably narrower widths, ranging only from 1000 to 4500 km s^{-1} . Of course, by originally selecting narrow C IV lines, we naturally identified targets at one extreme end of the line-width ratio distribution.

At least part of the broad emission lines in the UV are likely unobservable due to extinction. Whether the broadest components are preferentially obscured, leading to the narrow line widths, or whether we simply lack the S/N to find the extended (faint) broad wings is difficult to determine from these data. However, at least part of the broad-line region is directly transmitted in the UV. This broad component in C IV also explains the low ratios of He II to C IV reported in Paper I, which are consistent with broad-line rather than narrow-line objects (e.g., Nagao et al. 2006).

The targets presented here display broad $H\alpha$, and thus do not obey classic definitions of Type II active nuclei (e.g., Khachikyan & Weedman 1971). Furthermore, in general, the extinction associated with classical, optically selected Type II sources is larger than measured here. For lower luminosity Seyfert galaxies, A_V has been estimated using the ratios of $\text{Pa}\alpha$ to $H\alpha$, with values of more than 10 being common (e.g., Rix et al. 1990; Goodrich et al. 1994; Veilleux et al. 1997). In Type II quasars at $z \approx 0.5$, the weak continuum and lack of strong NIR emission suggests $A_B > 13$ (Zakamska et al. 2005). At more comparable redshifts to our targets, composite spectral energy distribution modeling of Type II AGN with a galaxy+AGN template yields similarly high values of $A_B > 13$ in most cases (e.g., Hickox et al. 2007; Mainieri et al. 2011; Hainline et al. 2012; Assef et al. 2013; Lusso et al. 2013). The obscuration levels reported here, in contrast, are comparable to those seen in so-called ‘‘Seyfert 1.8’’ galaxies (e.g., Osterbrock 1981; Rix et al. 1990), and the large ratios of narrow-to-broad line FWHM seen in $H\alpha$ are also characteristic of this moderately obscured class.

A more luminous population with interestingly similar characteristics are ‘‘red quasars,’’ selected as Type I reddened quasars in the rest-frame optical/NIR (e.g., Glikman et al. 2007; Urrutia et al. 2009, 2012; Banerji et al. 2012; Glikman et al. 2013; Banerji et al. 2013). When selected in the rest-frame optical/NIR, such objects make up $\sim 20\%$ of the quasar population (Glikman et al. 2012; Elitzur 2012). Like our targets, these so-called red quasars have moderate extinction, $A_V \approx 0.3-4.5 \text{ mag}$, such that broad $H\alpha$ is observed. Our targets are typically

more luminous in *WISE* by at least an order of magnitude than those in Glikman et al. (2012), but are also typically found at higher redshifts. The Banerji objects are selected from deeper NIR photometry and thus comprise somewhat more extincted ($A_V \approx 2-6$ mag) and more intrinsically luminous objects (by factors of a few) at comparable redshifts to ours. Eventually we will be able to compare these samples in the rest-frame UV as well (Glikman, private communication). Sources selected in the mid-IR (e.g., Dey et al. 2008; Stern et al. 2012; Assef et al. 2013) tend to be factors of a few more luminous in the MIR and redder than our rest-frame UV selected sample (e.g., Wu et al. 2012).

A few quasars with similarly moderate extinction inferred from the rest-frame optical/UV have also been uncovered in X-ray surveys, sometimes with significant obscuring columns in the X-ray (e.g., Almaini et al. 1995; Georgantopoulos et al. 1999, 2003; Piconcelli et al. 2005). X-ray spectroscopy of some of our quasars would allow the relative levels of X-ray and optical/UV obscuration to be assessed. Substantial apparent differences between such obscuration levels are often found, likely owing to the presence of some X-ray absorption within the dust-sublimation radius (e.g., Maiolino et al. 2001).

Obviously, each selection method imposes a preferred distribution of reddening and luminosity on the final sample. Assef et al. (2013) have recently measured a distribution of $E(B-V)$ for luminous *WISE*-selected quasars at $z < 1$. Interestingly, they find two natural breaks in the distribution. The first is at $E(B-V) \approx 0.15$, $A_V \approx 0.5$ mag, corresponding roughly to the sources observed here. They find a second transition at $E(B-V) \approx 2$, $A_V \approx 6$ mag. They postulate that the moderate extinction may arise on galaxy-wide scales while the second transition is due to the orientation of a dusty torus in the nucleus. Perhaps our *HST* imaging will allow us to distinguish these two scenarios for our candidates (Strauss et al. in prep.).

Taken altogether, our observations paint a nuanced picture of a mildly-obscured population of high-redshift quasars selected with the BOSS survey. How they fit into the broader picture of quasar demographics at this epoch remains to be seen. As a class of objects with obscuration intermediate between Type I and Type II sources, they may be at intermediate orientation in a unification picture, or just result from a patchy torus (e.g., Elitzur 2012). Alternatively, the host galaxy may

provide some large fraction of the obscuration, in an evolutionary picture (e.g., Sanders et al. 1988; Lacy et al. 2007; Hopkins et al. 2006). We may hope to get some clues to their star formation properties from higher S/N NIR spectra. We also have many more BOSS targets to study; the sample properties of the targets presented in Paper I are heterogeneous, and the faintest targets may yet harbor some bona-fide Type II quasars. We are also planning to obtain uniform NIR imaging, to preferentially select the faintest targets in the rest frame optical, which are most likely to be heavily obscured. Combining broad-band SED fitting, *HST* imaging, spectropolarimetry, and more NIR spectroscopy, may provide a more complete picture of the nature of these enigmatic targets.

We thank the referee for a very insightful report that improved the quality of this manuscript. We thank E. Glikman, G. Richards, R. Riffel, and G. Zhu for useful discussions, and gratefully thank the Gemini, Magellan, and APO staff who helped with both Phase II preparations and observations on the mountain. MAS and RA thank the support of NSF grant AST-0707266. Funding for SDSS-III has been provided by the Alfred P. Sloan Foundation, the Participating Institutions, the National Science Foundation, and the U.S. Department of Energy Office of Science. The SDSS-III web site is <http://www.sdss3.org/>.

SDSS-III is managed by the Astrophysical Research Consortium for the Participating Institutions of the SDSS-III Collaboration including the University of Arizona, the Brazilian Participation Group, Brookhaven National Laboratory, Carnegie Mellon University, University of Florida, the French Participation Group, the German Participation Group, Harvard University, the Instituto de Astrofísica de Canarias, the Michigan State/Notre Dame/JINA Participation Group, Johns Hopkins University, Lawrence Berkeley National Laboratory, Max Planck Institute for Astrophysics, Max Planck Institute for Extraterrestrial Physics, New Mexico State University, New York University, Ohio State University, Pennsylvania State University, University of Portsmouth, Princeton University, the Spanish Participation Group, University of Tokyo, University of Utah, Vanderbilt University, University of Virginia, University of Washington, and Yale University.

REFERENCES

- Ahn, C. P., Alexandroff, R., Allende Prieto, C., et al. 2012, *ApJS*, 203, 21
 Alexandroff, R., et al. 2013, *MNRAS*, 435, 3306
 Almaini, O., Boyle, B. J., Griffiths, R. E., et al. 1995, *MNRAS*, 277, L31
 Antonucci, R. 1993, *ARA&A*, 31, 473
 Antonucci, R. R. J., & Miller, J. S. 1985, *ApJ*, 297, 621
 Assef, R. J., et al. 2011, *ApJ*, 742, 93
 —. 2013, *ApJ*, 772, 26
 Banerji, M., McMahon, R. G., Hewett, P. C., et al. 2012, *MNRAS*, 427, 2275
 Banerji, M., McMahon, R. G., Hewett, P. C., Gonzalez-Solares, E., & Koposov, S. E. 2013, *MNRAS*, 429, L55
 Barger, A. J., et al. 2003, *AJ*, 126, 632
 Barth, A. J., Bentz, M. C., Greene, J. E., & Ho, L. C. 2008, *ApJ*, 683, L119
 Barth, A. J., et al. 2011, *ApJ*, 743, L4
 Becker, R. H., White, R. L., & Helfand, D. J. 1995, *ApJ*, 450, 559
 Bentz, M. C., Peterson, B. M., Netzer, H., Pogge, R. W., & Vestergaard, M. 2009, *ApJ*, 697, 160
 Bentz, M. C., et al. 2008, *ApJ*, 689, L21
 —. 2013, *ApJ*, 767, 149
 Berriman, G., Schmidt, G. D., West, S. C., & Stockman, H. S. 1990, *ApJS*, 74, 869
 Bolton, A. S., et al. 2012, *AJ*, 144, 144
 Bongiorno, A., et al. 2010, *A&A*, 510, A56
 Brandt, W. N., & Hasinger, G. 2005, *ARA&A*, 43, 827
 Brotherton, M. S., Wills, B. J., Francis, P. J., & Steidel, C. C. 1994, *ApJ*, 430, 495
 Canalizo, G., & Stockton, A. 2001, *ApJ*, 555, 719
 Comerford, J. M., Griffith, R. L., Gerke, B. F., et al. 2009, *ApJ*, 702, L82
 Cushing, M. C., Vacca, W. D., & Rayner, J. T. 2004, *PASP*, 116, 362
 Dawson, K. S., Schlegel, D. J., Ahn, C. P., et al. 2013, *AJ*, 145, 10
 Denney, K. D., et al. 2010, *ApJ*, 721, 715
 Dey, A., Soifer, B. T., Desai, V., et al. 2008, *ApJ*, 677, 943
 Djorgovski, S. G., Courbin, F., Meylan, G., et al. 2007, *ApJ*, 662, L1
 Donley, J. L., Rieke, G. H., Pérez-González, P. G., & Barro, G. 2008, *ApJ*, 687, 111
 Donley, J. L., et al. 2012, *ApJ*, 748, 142
 Dunkley, J., et al. 2009, *ApJS*, 180, 306
 Eisenhardt, P. R. M., Wu, J., Tsai, C.-W., et al. 2012, *ApJ*, 755, 173
 Eisenstein, D. J., Weinberg, D. H., Agol, E., et al. 2011, *AJ*, 142, 72
 Elias, J. H., Joyce, R. R., Liang, M., et al. 2006, in *Society of Photo-Optical Instrumentation Engineers (SPIE) Conference Series*, Vol. 6269, Society of Photo-Optical Instrumentation Engineers (SPIE) Conference Series
 Elitzur, M. 2012, *ApJ*, 747, L33
 Elmegreen, B. G., Bournaud, F., & Elmegreen, D. M. 2008, *ApJ*, 688, 67
 Förster Schreiber, N. M., et al. 2011, *ApJ*, 739, 45
 Gaskell, C. M., Goosmann, R. W., Antonucci, R. R. J., & Whysong, D. H. 2004, *ApJ*, 616, 147
 Georgantopoulos, I., Almaini, O., Shanks, T., et al. 1999, *MNRAS*, 305, 125

- Georgantopoulos, I., Georgakakis, A., Stewart, G. C., et al. 2003, *MNRAS*, 342, 321
- Georgantopoulos, I., et al. 2013, *A&A*, 555, A43
- Gilli, R., Comastri, A., & Hasinger, G. 2007, *A&A*, 463, 79
- Glikman, E., Helfand, D. J., White, R. L., et al. 2007, *ApJ*, 667, 673
- Glikman, E., et al. 2012, *ApJ*, 757, 51
- . 2013, *ApJ*, 778, 127
- Goad, M., & Koratkar, A. 1998, *ApJ*, 495, 718
- Goodrich, R. W., Veilleux, S., & Hill, G. J. 1994, *ApJ*, 422, 521
- Greene, J. E., & Ho, L. C. 2004, *ApJ*, 610, 722
- . 2005a, *ApJ*, 627, 721
- . 2005b, *ApJ*, 630, 122
- . 2006, *ApJ*, 641, L21
- . 2007, *ApJ*, 667, 131
- Greene, J. E., Peng, C. Y., & Ludwig, R. R. 2010, *ApJ*, 709, 937
- Greene, J. E., Zakamska, N. L., Ho, L. C., & Barth, A. J. 2011, *ApJ*, 732, 9
- Gunn, J. E., et al. 2006, *AJ*, 131, 2332
- Hainline, K. N., Shapley, A. E., Greene, J. E., & Steidel, C. C. 2011, *ApJ*, 733, 31
- Hainline, K. N., Shapley, A. E., Greene, J. E., et al. 2012, *ApJ*, 760, 74
- Hamann, F., Shields, J. C., Ferland, G. J., & Korista, K. T. 1995, *ApJ*, 454, 688
- Hao, L., et al. 2005, *AJ*, 129, 1783
- Hasinger, G. 2008, *A&A*, 490, 905
- Heckman, T. M., et al. 2004, *ApJ*, 613, 109
- Hewett, P. C., Warren, S. J., Leggett, S. K., & Hodgkin, S. T. 2006, *MNRAS*, 367, 454
- Hickox, R. C., et al. 2007, *ApJ*, 671, 1365
- Ho, L. C. 2005, *ApJ*, 629, 680
- Ho, L. C., Filippenko, A. V., Sargent, W. L. W., & Peng, C. Y. 1997, *ApJS*, 112, 391
- Ho, L. C., Goldoni, P., Dong, X.-B., Greene, J. E., & Ponti, G. 2012, *ApJ*, 754, 11
- Hopkins, P. F., Hernquist, L., Cox, T. J., et al. 2006, *ApJS*, 163, 1
- Hopkins, P. F., et al. 2004, *AJ*, 128, 1112
- Ilbert, O., et al. 2009, *ApJ*, 690, 1236
- Iwasawa, K., et al. 2012, *A&A*, 546, A84
- Kashi, A., Proga, D., Nagamine, K., Greene, J., & Barth, A. J. 2013, *ApJ*, 778, 50
- Kaspi, S., Smith, P. S., Netzer, H., et al. 2000, *ApJ*, 533, 631
- Kelly, B. C., Vestergaard, M., & Fan, X. 2009, *ApJ*, 692, 1388
- Kelson, D. D. 2003, *PASP*, 115, 688
- Khachikyan, E. Y., & Weedman, D. W. 1971, *Astrophysics*, 7, 231
- Korista, K. T., & Goad, M. R. 2004, *ApJ*, 606, 749
- Kramida, A., Yu. Ralchenko, Reader, J., & and NIST ASD Team. 2013, NIST Atomic Spectra Database (ver. 5.1), [Online]. Available: <http://physics.nist.gov/asd> [2013, December 29]. National Institute of Standards and Technology, Gaithersburg, MD.
- Krolik, J. H. 2001, *ApJ*, 551, 72
- Lacy, M., et al. 2004, *ApJS*, 154, 166
- . 2007, *ApJ*, 669, L61
- . 2013, *ApJS*, 208, 24
- Lawrence, A., et al. 2007, *MNRAS*, 379, 1599
- Liu, G., Zakamska, N. L., & Greene, J. E. 2014, *MNRAS*, submitted (arXiv:1401.0536), arXiv:1401.0536
- Liu, G., Zakamska, N. L., Greene, J. E., Nesvadba, N. P. H., & Liu, X. 2013a, *MNRAS*, 430, 2327
- . 2013b, *MNRAS*, 436, 2576
- Liu, X., Shen, Y., & Strauss, M. A. 2011, *ApJ*, 736, L7
- Liu, X., Shen, Y., Strauss, M. A., & Greene, J. E. 2010, *ApJ*, 708, 427
- Liu, X., Zakamska, N. L., Greene, J. E., et al. 2009, *ApJ*, 702, 1098
- Lusso, E., et al. 2013, *ApJ*, 777, 86
- MacAlpine, G. M. 1985, in *Astrophysics of Active Galaxies and Quasi-Stellar Objects*, ed. J. S. Miller, 259–288
- Mainieri, V., et al. 2011, *A&A*, 535, A80
- Maiolino, R., Marconi, A., Salvati, M., et al. 2001, *A&A*, 365, 28
- Markwardt, C. B. 2009, in *Astronomical Society of the Pacific Conference Series*, Vol. 411, *Astronomical Data Analysis Software and Systems XVIII*, ed. D. A. Bohlender, D. Durand, & P. Dowler, 251
- Matsuoka, K., et al. 2013, *ApJ*, 771, 64
- McCarthy, P. J. 1993, *ARA&A*, 31, 639
- Mignoli, M., et al. 2013, *A&A*, 556, A29
- Nagao, T., Maiolino, R., & Marconi, A. 2006, *A&A*, 447, 863
- Nenkova, M., Sirocky, M. M., Nikutta, R., Ivezić, Ž., & Elitzur, M. 2008, *ApJ*, 685, 160
- Netzer, H., et al. 2005, *ApJ*, 629, 739
- Norman, C., et al. 2002, *ApJ*, 571, 218
- Oke, J. B., & Gunn, J. E. 1983, *ApJ*, 266, 713
- Osterbrock, D. E. 1981, *ApJ*, 249, 462
- Osterbrock, D. E., & Pogge, R. W. 1985, *ApJ*, 297, 166
- Page, M. J., Stevens, J. A., Mittaz, J. P. D., & Carrera, F. J. 2001, *Science*, 294, 2516
- Pancoast, A., et al. 2012, *ApJ*, 754, 49
- Pâris, I., Petitjean, P., Aubourg, É., et al. 2012, *A&A*, 548, A66
- Pei, Y. C. 1992, *ApJ*, 395, 130
- Piconcelli, E., Guainazzi, M., Cappi, M., Jimenez-Bailon, E., & Schartel, N. 2005, *A&A*, 432, 835
- Reines, A. E., Greene, J. E., & Geha, M. 2013, *ApJ*, 775, 116
- Reyes, R., et al. 2008, *AJ*, 136, 2373
- Richards, et al. 2006, *AJ*, 131, 2766
- Rigby, J. R., Rieke, G. H., Donley, J. L., Alonso-Herrero, A., & Pérez-González, P. G. 2006, *ApJ*, 645, 115
- Rix, H.-W., Rieke, G., Rieke, M., & Carleton, N. P. 1990, *ApJ*, 363, 480
- Ross, N. P., et al. 2012, *ApJS*, 199, 3
- . 2013, *ApJ*, 773, 14
- Sanders, D. B., Soifer, B. T., Elias, J. H., et al. 1988, *ApJ*, 325, 74
- Scoville, N., Aussel, H., Brusa, M., et al. 2007, *ApJS*, 172, 1
- Shapley, A. E. 2011, *ARA&A*, 49, 525
- Shen, Y. 2013, *Bulletin of the Astronomical Society of India*, 41, 61
- Shen, Y., Greene, J. E., Strauss, M. A., Richards, G. T., & Schneider, D. P. 2008, *ApJ*, 680, 169
- Shen, Y., & Liu, X. 2012, *ApJ*, 753, 125
- Shen, Y., et al. 2011, *ApJS*, 194, 45
- Simcoe, R. A., Sullivan, P. W., Cooksey, K. L., et al. 2012, *Nature*, 492, 79
- Simcoe, R. A., et al. 2013, *PASP*, 125, 270
- Smee, S. A., et al. 2013, *AJ*, 146, 32
- Steffen, A. T., et al. 2003, *ApJ*, 596, L23
- Steidel, C. C., Hunt, M. P., Shapley, A. E., et al. 2002, *ApJ*, 576, 653
- Stern, D., et al. 1999, *AJ*, 117, 1122
- . 2002, *ApJ*, 568, 71
- Stern, D., Eisenhardt, P., Gorjian, V., et al. 2005, *ApJ*, 631, 163
- Stern, D., et al. 2012, *ApJ*, 753, 30
- Stevens, J. A., Page, M. J., Ivison, R. J., et al. 2005, *MNRAS*, 360, 610
- Ueda, Y., Akiyama, M., Ohta, K., & Miyaji, T. 2003, *ApJ*, 598, 886
- Urrutia, T., Becker, R. H., White, R. L., et al. 2009, *ApJ*, 698, 1095
- Urrutia, T., Lacy, M., & Becker, R. H. 2008, *ApJ*, 674, 80
- Urrutia, T., Lacy, M., Spoon, H., et al. 2012, *ApJ*, 757, 125
- Urry, C. M., & Padovani, P. 1995, *PASP*, 107, 803
- Vacca, W. D., Cushing, M. C., & Rayner, J. T. 2003, *PASP*, 115, 389
- Vanden Berk, D., et al. 2008, *ApJ*, 679, 239
- Veilleux, S., Goodrich, R. W., & Hill, G. J. 1997, *ApJ*, 477, 631
- Veilleux, S., et al. 2009, *ApJ*, 701, 587
- Vestergaard, M. 2002, *ApJ*, 571, 733
- Vestergaard, M., & Peterson, B. M. 2006, *ApJ*, 641, 689
- Wilson, J. C., et al. 2004, in *Society of Photo-Optical Instrumentation Engineers (SPIE) Conference Series*, Vol. 5492, *Society of Photo-Optical Instrumentation Engineers (SPIE) Conference Series*, ed. A. F. M. Moorwood & M. Iye, 1295–1305
- Wu, J., et al. 2012, *ApJ*, 756, 96
- Xue, Y. Q., et al. 2012, *ApJ*, 758, 129
- Yan, L., et al. 2013, *AJ*, 145, 55
- Yee, H. K. C. 1980, *ApJ*, 241, 894
- York, D. G., Adelman, J., Anderson, J. J. E., et al. 2000, *AJ*, 120, 1579
- York, D. G., et al. 2006, *MNRAS*, 367, 945
- Zakamska, N. L., Gómez, L., Strauss, M. A., & Krolik, J. H. 2008, *AJ*, 136, 1607
- Zakamska, N. L., et al. 2003, *AJ*, 126, 2125
- . 2005, *AJ*, 129, 1212
- Zakamska, N. L., Strauss, M. A., Krolik, J. H., et al. 2006, *AJ*, 132, 1496